Echoes from bounded universes

Renan B. Magalhães,[1,2,*] Andreu S. Masó-Ferrando,[2,†] Flavio Bombacigno,[2,‡] Gonzalo J. Olmo,[2,§] and Luís C. B. Crispino[1,‖]

[1]*Programa de Pós-Graduação em Física, Universidade Federal do Pará, 66075-110 Belém, Pará, Brazil*
[2]*Departamento de Física Teórica and IFIC, Centro Mixto Universidad de Valencia—CSIC, Universidad de Valencia, Burjassot-46100, Valencia, Spain*

(Received 22 November 2023; revised 14 June 2024; accepted 16 July 2024; published 28 August 2024)

We construct a general class of modified Ellis-Bronnikov wormholes, where one asymptotic Minkowski region is replaced by a bounded 2-sphere core, characterized by an asymptotic finite areal radius. We pursue an in-depth analysis of the resulting geometry, outlining that geodesic completeness is also guaranteed when the area function asymptotically shrinks to zero. Moreover, we perform an analysis of the circular orbits present in our model and conclude that stable circular orbits are allowed in the bounded region. As a consequence, a stable light ring may exist in the inner region and trapped orbits may appear within this bounded region. Such internal structure suggests that the bounded region can trap perturbations. Then, we study the evolution of scalar perturbations, bringing out how these geometric configurations can in principle affect the time-domain profiles of quasinormal modes, pointing out the distinctive features with respect to other black hole or wormhole geometries.

DOI: 10.1103/PhysRevD.110.044058

I. INTRODUCTION

The advent of gravitational wave astronomy [1] and the technical progress made in very large base-line interferometry [2] is enabling us to confront predictions of gravitational theories in the strong field regime with observational data. In this sense, significant theoretical efforts are being devoted to the search and study of exotic compact objects that may offer a reasonable alternative to the black hole paradigm of Einstein's theory of general relativity (GR). Such objects could lead to effects not expected in GR and, for this reason, their analysis could help identify observational signatures of new physics. Among the most popular alternatives, one finds hairy or regularized black holes [3–6], boson stars [7,8], gravastars [9], wormholes [10], and black bounces [11]. In this work, we put the focus on a new kind of exotic object closely related with wormholes but with proper observational features that could allow us to tell them apart from the usual wormholes found in the literature.

In the conventional approach to the resolution of the field equations of a given gravitational system, one typically begins with a reasonable description of the matter sources and then employs the Einstein field equations to derive the corresponding spacetime geometry. When dealing with wormhole configurations, however, the process is usually inverted. In fact, once the desired spacetime geometry is selected, it is possible to use Einstein's equations in reverse to determine the matter distribution responsible for it. Despite violating various energy conditions, wormholes still stand out because of their theoretical implications, as they offer valuable insights into the foundational aspects of gravity models and their possible nontrivial topological structure. Wormholes are not only relevant for interstellar travel [12], which is a well-known and popular application recurrently used in the literature, but could also be crucial to better understand the nature of quantum entanglement [13]. For these reasons, it is important to explicitly address the theoretical implications of their existence and the proper observational signatures that could signal their presence in astrophysical scenarios [14–20].

The emission of gravitational waves by the coalescence of compact objects, for instance, can clearly distinguish between black holes (objects with an event horizon) and wormholes (no event horizon), as the latter are expected to emit a series of echoes [21] which are not present in the case of objects with a horizon, from which nothing can come out (though these echoes are not unique to wormholes; see for instance [22]). Also, the distortion of light trajectories by black holes and wormholes might be quite different, not only because wormholes may allow light to come out from their internal region but also because the number and structure of light rings might exhibit different behaviors [23,24]. These aspects can be used to identify a

*Contact author: renan.magalhaes@icen.ufpa.br
†Contact author: andreu.maso@uv.es
‡Contact author: flavio2.bombacigno@uv.es
§Contact author: gonzalo.olmo@uv.es
‖Contact author: crispino@ufpa.br

number of treats that allow to characterize the various specimens present in the zoo of compact objects.

In this sense, it should be noted that among the billions of compact objects present in the Universe, the observation of events apparently compatible with our predictions does not rule out the existence of objects of a different nature. Current detectors' sensitivities are still insufficient to break significant degeneracies in the data [25], which demands new generations of observatories able to provide a clearer picture of the nature of such objects [26]. In the meantime, the existence and consistency of exotic compact objects can be pursued theoretically, with the aim of identifying their proper signatures and potential phenomenological implications.

It is important, therefore, to have a clear understanding of the proper features that define and identify wormholes. From an astrophysical perspective, one would expect that wormholes should be spherical or axisymmetric (rotating). Accordingly, the presence of spherically symmetric wormholes is typically identified in the literature by the existence of a 2-sphere of minimal nonzero area, which represents the wormhole throat [10,27]. However, the observation of a minimal 2-sphere, which is a local characteristic, cannot be used to infer anything about the global properties of the spacetime, such as its topology. Thus, in order to broaden our understanding of their observational features, it is necessary to consider scenarios in which typical local properties of wormholes are present but where their proper global aspects are not. In particular, since in standard wormholes the throat connects two unbounded regions (typically asymptotically flat, though there are exceptions [28,29]), one may consider spacetimes where the throat connects an unbounded region to a bounded one. Spacetimes with this characteristic have been recently found as the end product of the collapse of boson stars in quadratic Palatini gravity [30,31]. In that scenario, the central region of the collapsed object experiences a kind of inflationary stretching that leads to the formation of an expanding bubble (or baby universe) behind the event horizon. Inspired by that phenomenon, here we consider a static setting in which an asymptotically Minkowskian region is attached to a bounded bubble via a minimal 2-sphere. The gravitational echoes generated by such bounded universes and their geodesic structure will be scrutinized and compared with those of more standard wormholes.

One of the simplest wormhole configurations is represented by the well-known Ellis-Bronnikov wormhole (EBWH) [32,33], which is made of two asymptotically flat regions connected by a throat.[1] In this work we introduce the idea that one of the infinite asymptotic regions, i.e. the Minkowski spacetime of EBWHs, could be possibly replaced by some inner spatial volume endowed with finiteness in one or more directions. The (partial) compactness of this new internal region is thus expected to induce specific observable effects on both the shadow of the object and on its spectroscopic properties, where peculiar absorption effects, resonances, and echoes may arise depending on the typical size of the internal region and the different boundary conditions involved.

In this work we take a first step in this direction by looking at minimal deformations of the classic EBWH [32] considering that one of the asymptotic Minkowski regions is replaced by a bounded 2-sphere with asymptotically constant areal radius. We expect that the finiteness of the radial function in this internal region plays a relevant role in the propagation of perturbations, because the effective potential perceived by scalar modes, hereinafter V_Φ, critically depends on the areal radius behavior. In particular, we refer to the possibility that echoes could be generated, bringing the question of how to distinguish, in a phenomenological sense, our geometrical setting from analogous results in different scenarios [35–40]. Moreover, among the possible geometric realizations studied, we consider the case in which the asymptotic areal radius vanishes, implying that the geodesic completeness of the resulting spacetime is not *a priori* guaranteed (see [41,42] for examples of geodesically incomplete wormholes). In order to clarify this delicate issue we analyze to some extent the geodesic motion for radial (analytically) and nonradial (numerically) trajectories, confirming that geodesic completeness is insensitive to the actual value of the asymptotic areal radius, which turns out to affect only the presence or not of inner region bounces for nonradial motion.

The paper is organized as follows. In Sec. II we introduce the model and we discuss the general geometric properties, by also presenting a detailed analysis of the energy condition violation; in Sec. III we perform an exhaustive investigation of geodesic motion and photon orbit stability; in Sec. IV scalar perturbations are addressed and we show how the appearance and the properties of echoes are affected by the geometry; and in Sec. V we report our final comments.

The spacetime signature is chosen mostly plus, i.e. $\eta_{\mu\nu} = \mathrm{diag}(-1, 1, 1, 1)$ and we adopt units in which $G = c = 1$.

II. THE MODEL

One of the simplest (symmetric) traversable wormholes in the literature is represented by the EBWH, whose line element is given by [32,33]

$$ds^2 = -dt^2 + dx^2 + r^2(x)(d\theta^2 + \sin^2\theta d\varphi^2), \qquad (1)$$

with radial coordinate $x \in (-\infty, \infty)$ and areal radius $r(x) = \sqrt{x^2 + a^2}$. The areal radius has a regular minimum at $x = 0$, which corresponds to the wormhole throat with radius a. The throat separates the spacetime into two

[1] In this work we do not focus on wormhole geometries involving Schwarzschild-like deformation (see for instance [11]), which will be the subject of a forthcoming analysis [34].

symmetric regions, called respectively the inner (or internal) region for $x < 0$ and outer (or external) region for $x > 0$. As $|x|$ increases, the areal radius monotonically grows and the line element (1) approaches Minkowski spacetime as $x \to \pm\infty$.

Here we present a toy model of a wormhole-like object with an inner region characterized by a maximal 2-sphere and an asymptotically flat exterior, formally described by the line element (1), but with a modified radial function $r(x)$ that accounts for the inner structure. This asymmetric configuration is achieved by requiring:

(i) *The smoothness of the throat*

$$\lim_{x\to 0} r(x) = a, \qquad \lim_{x\to 0} \frac{dr}{dx} = 0, \qquad \lim_{x\to 0} \frac{d^2 r}{dx^2} = \frac{1}{a}; \tag{2}$$

(ii) *The asymptotic boundedness of the internal region*

$$\lim_{x\to -\infty} r(x) = R; \tag{3}$$

where a and R are non-negative constants with dimension of length, which denote the throat radius and the (internal) bounded 2-sphere radius, respectively. Assumption (2) guarantees a smooth local minimum in the areal radius, assuring the presence of a throat structure in the spacetime and, additionally, a smooth transition from the external to the internal region. In turn, assumption (3) imposes that, as one moves towards the internal region, the spacetime evolves into a finite 2-sphere core. Under these conditions, one has a large freedom to choose the areal radius profile, and here we propose a model with

$$r^2(x) = \begin{cases} x^2 + a^2, & x \geq 0, \\ (x^2 + a^2)\mathrm{sech}^2(cx^2) + R^2 \tanh^2(cx^2), & x < 0, \end{cases} \tag{4}$$

where c is a non-negative constant with dimension of length^{-2}. The advantage of this toy model is the simpler dependences on parameters governing the internal boundedness.

One can check that (4) is endowed with a throat-like structure in $x = 0$, where $r(x)$ exhibits the regular minimum $r^2(0) = a^2$. In the asymptotic internal region, as $x \to -\infty$, the radial function $r^2(x) \to R^2$, that is, the 2-sphere radius is asymptotically bounded. The role of the parameter c is to control how much the radial function $r^2(x)$ departs from a parabola close to the throat, so that the asymptotic value R is reached faster as one increases the value of c. If $c = 0$, the radial function (4) reduces to that of the EBWH, that is, $r^2(x) = x^2 + a^2$.

In this model, the outer universe ($x \geq 0$) is described by the same line element as the EBWH spacetime. The modified areal radius (4), however, sharply modifies the structure of the inner universe ($x < 0$). In Fig. 1 we exhibit

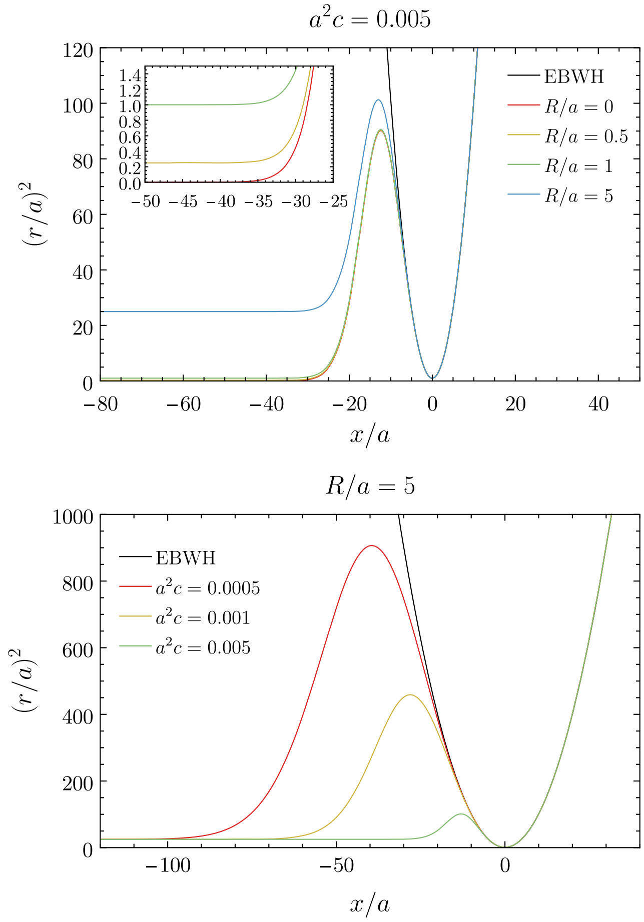

FIG. 1. Modified areal radius (4). Top panel: $r^2(x)$ for fixed value of c and different asymptotic 2-sphere radius R. Bottom panel: $r^2(x)$ for fixed R and some choices of c. We normalize the plots with the throat radius a.

the behavior of the modified areal radius squared on both sides of the throat and compare it with the standard parabolic behavior of EBWH ($r^2(x) = x^2 + a^2$). In the top panel we fix the value of the parameter c and consider some values of the asymptotic 2-sphere radius R. In the bottom panel we fix the asymptotic radius and consider different values of c. From Fig. 1 one notices that the areal radius may present a local maximum in the inner region. One can check that the location of the maximum, x_m, must satisfy $M(x_m) = 0$ and $r_{xx}(x_m) < 0$, where $r_x \propto M(x)$, with

$$M(x) \equiv 1 - 2c(x^2 + a^2 - R^2)\tanh(cx^2) \tag{5}$$

where r_x and r_{xx} stand for the first and second derivatives of $r(x)$ with respect to x. Since $M(x)$ is continuous in the interval $(-\infty, 0)$, and $M(x) \to -\infty$ as $x \to -\infty$ and $M(x) \to 1$ as $x \to 0^-$, there is at least one point $x_m \in (-\infty, 0)$ such that $M(x_m) = 0$, and this point is a maximum if $r_{xx}(x_m) < 0$.

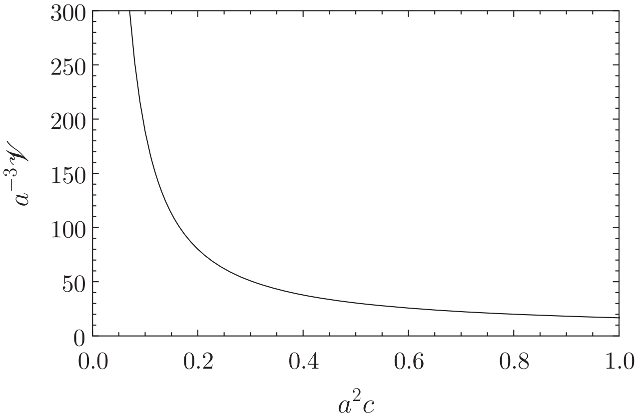

FIG. 2. Finite volume of the internal region of the modified EBWH with $R = 0$ as a function of c.

In the particular case when $R = 0$, the 2-sphere radius shrinks to zero exponentially fast (cf. Fig. 1), and one can say that the internal region is *effectively* closed spatially. To better see this, one can compute the volume of the inner region by following [43] (see also [44] for equivalent definitions of spacetime volume) as

$$\begin{aligned}\mathcal{V} &= \int_{\mathcal{B}} \sqrt{-g}\,dx d\theta d\varphi \\ &= \int_0^{2\pi} d\varphi \int_0^{\pi} \sin\theta d\theta \int_{-\infty}^{0} (x^2 + a^2)\mathrm{sech}^2(cx^2)dx, \end{aligned} \quad (6)$$

where $\mathcal{B}$ denotes the three-dimensional region behind the throat. One notes that if $c = 0$ the volume $\mathcal{V}$ blows up, since in this case the internal (as well as the external) region of the EBWH is infinite. Conversely, for nonvanishing values of c, the internal volume $\mathcal{V}$ is finite. In Fig. 2 we plot $\mathcal{V}$ as a function of the parameter c.

A. Embedding diagrams

The areal function (4), therefore, significantly changes the structure of the modified EBWH internal region. This can be properly visualized by drawing the embedding diagrams of the model for different asymptotic 2-sphere radii. To do so, we consider at a given time coordinate t the equatorial plane $\theta = \pi/2$, where the metric (1) reduces to $ds^2 = dx^2 + r^2(x)d\phi^2$. Now, one may embed this hypersurface in the three-dimensional Euclidean space (written in cylindrical coordinates) $ds^2 = dz^2 + d\rho^2 + \rho^2 d\phi^2$. By identifying the polar radius with the radial function, i.e. $\rho = r(x)$, one obtains the differential equation

$$z_x^2 = 1 - r_x^2, \quad (7)$$

which can be solved for $z(x)$. Together with (4), they can be plotted in the plane $r - z$ to build the embedding diagram as the revolution surface of the curve $\gamma(x) = (r(x), z(x))$ about the axis $r = 0$. In Fig. 3 we show the embedding diagrams of two bounded EBWHs. In the top panel, we find the object whose 2-sphere radius shrinks to zero in the asymptotic region, creating a sort of "bubble" below the throat, which makes evident the finiteness of this spatial volume, as computed via Eq. (6). When the internal sector tends to a constant area (lower panel), the spatial volume is clearly infinite. Though we are mainly interested in asymmetric configurations of a bounded 2-sphere connected to an asymptotically flat region (where observers are expected to live), for the sake of completeness we also show in Fig. 4 two symmetric bounded configurations.

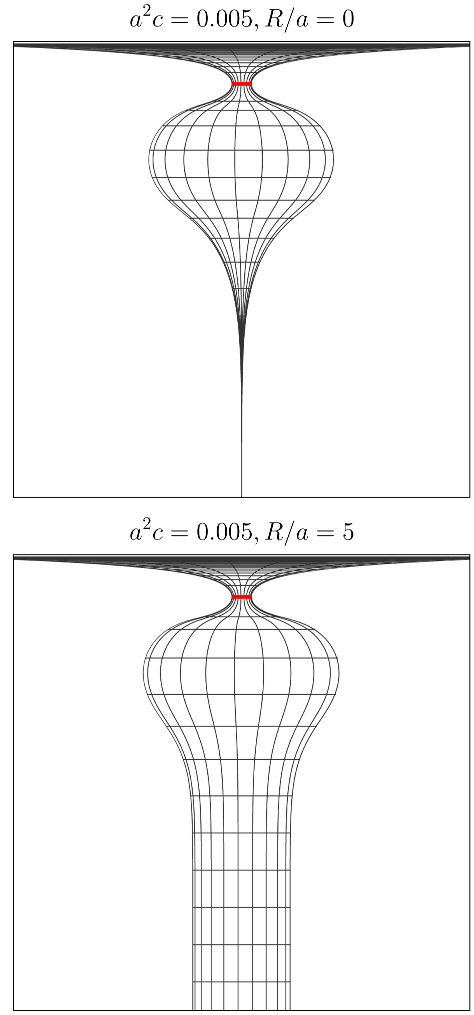

FIG. 3. Embedding diagrams of finite 2-sphere radius EBWHs with a fixed value of c. In the top panel we exhibit a wormhole-like object in which the 2-sphere radius shrinks to zero, creating a sort of "bubble" in the internal region, while in the bottom panel we show a configuration in which the asymptotic 2-sphere radius is bigger than the wormhole throat a.

B. Curvature, energy density and pressures

To have a better physical view of the solutions modeled by the line element (1) with areal radius (4), one can compute the curvature invariants related to it, which read

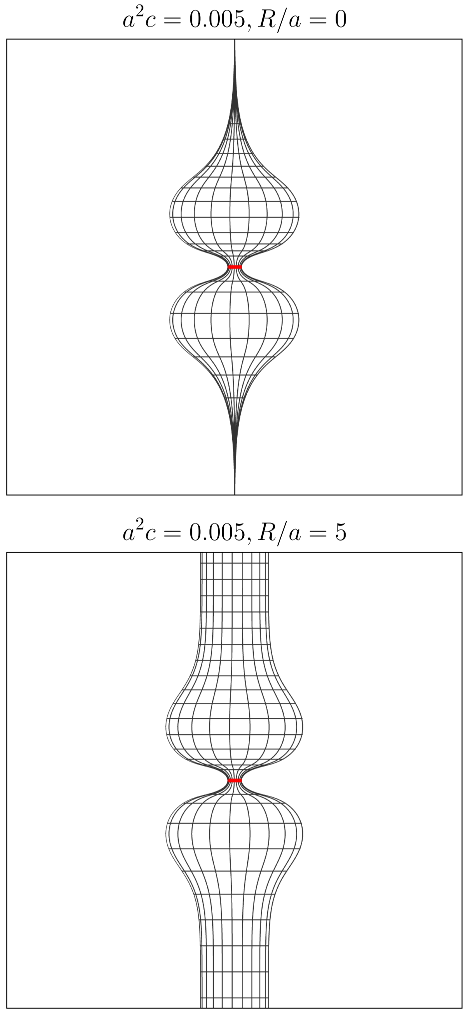

FIG. 4. Embedding diagrams of symmetric bounded wormholes with areal radius given by $r^2 = (x^2 + a^2)\mathrm{sech}^2(cx^2) + R^2\tanh^2(cx^2)$ in the two sides of the throat.

$$g_{\mu\nu}R^{\mu\nu} = \frac{2(1 - r_x^2 - 2rr_{xx})}{r^2}, \tag{8}$$

$$R_{\mu\nu}R^{\mu\nu} = \frac{2((r_x^2 - 1)^2 + 2r(r_x^2 - 1)r_{xx} + 3r^2 r_{xx}^2)}{r^4}, \tag{9}$$

$$R_{\alpha\beta\gamma\lambda}R^{\alpha\beta\gamma\lambda} = \frac{4(1 - 2r_x^2 + r_x^4 + 2r^2 r_{xx}^2)}{r^4}. \tag{10}$$

Since the spacetime is asymptotically flat in the exterior region, all the above curvature scalars vanish very far from the throat. In the internal region, instead, curvature invariants may be bounded or unbounded depending on the asymptotic 2-sphere radius R. As the radial coordinate approaches $x \to -\infty$, one finds that $g_{\mu\nu}R^{\mu\nu} \to 2/R^2$, $R_{\mu\nu}R^{\mu\nu} \to 2/R^4$ and $R_{\alpha\beta\gamma\lambda}R^{\alpha\beta\gamma\lambda} \to 4/R^4$, corresponding to the curvature invariants of a 2-sphere of radius R. If $R = 0$ the curvature scalars are unbounded in the internal region, as they diverge as $x \to -\infty$. However, as we will see, such a behavior does not actually represent any pathology in the spacetime, since all the geodesics can be extended forever in this geometry, and no spacetime singularity is present (see discussion in Sec. III). In Fig. 5 we show the curvature scalars of the modified EBWH. We notice that in the asymptotic internal region, the modified EBWH has the constant curvature of a 2-sphere of radius R and, in particular, the curvature scalars are unbounded if $R = 0$.

It is a well established fact that standard EBWHs can be sustained in GR only by the presence of exotic matter fields, resulting in the explicit violation of the different energy conditions [12,45]. Here, we show that our modified EBWH model, considered in the context of GR, does not evade such a restriction in the bounded region, and exotic matter sources are still required.[2] For this purpose, it is convenient to introduce the orthonormal frame

$$\mathbf{e}_{\hat{t}} = \partial_t, \qquad \mathbf{e}_{\hat{x}} = \partial_x, \qquad \mathbf{e}_{\hat{\theta}} = \frac{\partial_\theta}{r(x)}, \qquad \mathbf{e}_{\hat{\phi}} = \frac{\partial_\phi}{r(x)\sin\theta}, \tag{11}$$

which satisfies $g_{\mu\nu}e^\mu_{\hat{a}}e^\nu_{\hat{b}} = \eta_{\hat{a}\hat{b}}$, where $\eta_{\hat{a}\hat{b}} \equiv \mathrm{diag}(-1,1,1,1)$ is the Minkowski metric. In such a frame, the Einstein tensor takes the form $G_{\hat{a}\hat{b}} = G_{\mu\nu}e^\mu_{\hat{a}}e^\nu_{\hat{b}}$, whose components are

$$G_{\hat{t}\hat{t}} = \frac{1 - r_x^2 - 2r_{xx}}{r^2}, \tag{12}$$

$$G_{\hat{x}\hat{x}} = \frac{r_x^2 - 1}{r^2}, \tag{13}$$

$$G_{\hat{\theta}\hat{\theta}} = G_{\hat{\phi}\hat{\phi}} = \frac{r_{xx}}{r}. \tag{14}$$

By assuming for the source of the wormhole a fluid description, in the orthonormal basis we can write the energy-momentum tensor in the form $T_{\hat{a}\hat{b}} = \mathrm{diag}(\rho(x), -\tau(x), p(x), p(x))$, where its components have a well-known physical interpretation in terms of the energy density $\rho(x)$, the radial tension $\tau(x)$ and the lateral pressure $p(x)$. Now, requiring that our model is a solution of GR, i.e. $G_{\hat{a}\hat{b}} = 8\pi T_{\hat{a}\hat{b}}$, we obtain the expressions[3]

$$\rho = \frac{1 - r_x^2 - 2rr_{xx}}{8\pi r^2}, \qquad \tau = \frac{1 - r_x^2}{8\pi r^2}, \qquad p = \frac{r_{xx}}{8\pi r}, \tag{15}$$

with $\rho = -2p + \tau$. In the unbounded region, these quantities read

[2] Here we do not discuss in detail modified theories of gravity, where traversable wormhole configurations can emerge in the absence of exotic matter sources [46–54].

[3] Henceforth we omit the dependence on x in the components of the energy-momentum tensor.

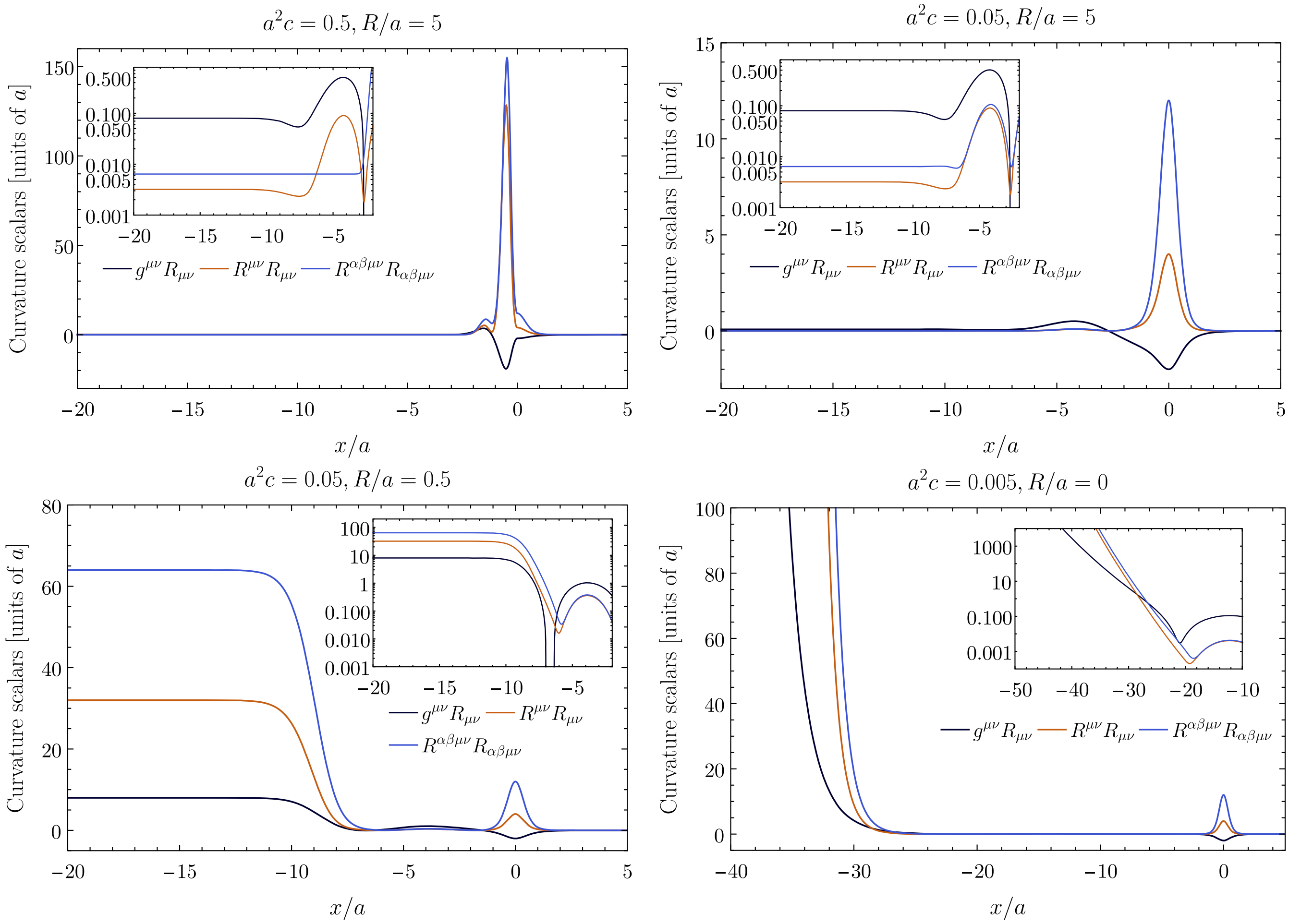

FIG. 5. Curvature scalars of the modified EBWH. One notes that the curvature scalars approach those of a 2-sphere of radius R in the asymptotic internal region. In particular the curvature scalars are unbounded in the vanishing R case.

$$\rho = -\frac{a^2}{8\pi(x^2 + a^2)^2}, \tag{16}$$

$$\tau = \frac{a^2}{8\pi(x^2 + a^2)^2}, \tag{17}$$

$$p = \frac{a^2}{8\pi(x^2 + a^2)^2}, \tag{18}$$

while in the bounded region they take much more cumbersome expressions

$$\begin{aligned}\rho = {} & \frac{4\cosh(2cx^2)(a^2(1 - 16c^2R^2x^2) + 2R^2(8c^2x^2(R - x)(R + x) - 1) + x^2)}{16\pi(2a^2 + R^2\cosh(2cx^2) - R^2 + 2x^2)^2} \\ & + \frac{16cR^2(a^2 - R^2 + 5x^2)\sinh(2cx^2) - 12a^2 + 7R^2 - 4x^2 + R^2\cosh(4cx^2)}{16\pi(2a^2 + R^2\cosh(2cx^2) - R^2 + 2x^2)^2} \\ & + \frac{c(a^2 - R^2 + x^2)\mathrm{sech}^2(cx^2)(a^2 - R^2 + 4x^2)\sinh(2cx^2)}{\pi(2a^2 + R^2\cosh(2cx^2) - R^2 + 2x^2)^2} \\ & + \frac{cx^2((-3a^2 + 7R^2 - 3x^2)\cosh(2cx^2) + 7a^2 - 3R^2 + 7x^2)}{\pi(2a^2 + R^2\cosh(2cx^2) - R^2 + 2x^2)^2\mathrm{sech}^2(cx^2)},\end{aligned} \tag{19}$$

$$\tau = \frac{\cosh^2(cx^2)(2a^2 + R^2\cosh(2cx^2) - R^2 + 2x^2) - (x - 2cx(a^2 - R^2 + x^2)\tanh(cx^2))^2}{4\pi(2a^2 + R^2\cosh(2cx^2) - R^2 + 2x^2)^2}, \tag{20}$$

$$p = \frac{R^2\cosh(2cx^2)(8c^2x^2(a^2-R^2+x^2)+1)+2cR^2(-a^2+R^2-5x^2)\sinh(2cx^2)}{4\pi(2a^2+R^2\cosh(2cx^2)-R^2+2x^2)^2} - \frac{4c(a^2-R^2+x^2)((a^2-R^2+3x^2)\tanh(cx^2)+2cx^2(2(a^2-R^2+x^2)\mathrm{sech}^2(cx^2)))}{4\pi(2a^2+R^2\cosh(2cx^2)-R^2+2x^2)^2} - \frac{4c(a^2-R^2+x^2)((-a^2+3R^2-x^2))+2a^2-R^2}{4\pi(2a^2+R^2\cosh(2cx^2)-R^2+2x^2)^2}. \quad (21)$$

If $R \neq 0$, it is easier to study the behavior of these quantities by analyzing Eq. (15), where it is clear that the energy density, radial tension and lateral pressure are finite or zero in the whole spacetime. In particular, in the asymptotic internal region they become

$$\lim_{x\to-\infty}\rho = \frac{1}{8\pi R^2}, \quad (22)$$

$$\lim_{x\to-\infty}\tau = \frac{1}{8\pi R^2}, \quad (23)$$

$$\lim_{x\to-\infty}p = 0. \quad (24)$$

When $R \to 0$, these fluid quantities are unbounded in the internal region. Expanding these functions, we find that their leading terms in the asymptotic internal region are

$$\rho_0 \approx \frac{1}{32\pi}\frac{e^{2cx^2}}{x^2} - \frac{3c^2x^2}{2\pi}, \quad (25)$$

$$\tau_0 \approx \frac{1}{32\pi}\frac{e^{2cx^2}}{x^2} - \frac{c^2x^2}{2\pi}, \quad (26)$$

$$p_0 \approx \frac{c^2x^2}{2\pi}, \quad (27)$$

where we have added a 0 subscript to emphasize that those quantities represent the limits when $R = 0$. One readily sees that the density and radial tension diverge more rapidly than the lateral pressure as $x \to -\infty$.

In GR, energy conditions may be posed in terms of the energy-momentum tensor components in the above orthonormal system [55,56]. They are the null energy condition

$$\rho - \tau \geq 0 \quad \text{and} \quad \rho + p \geq 0, \quad (28)$$

the weak energy condition

$$\rho \geq 0, \qquad \rho - \tau \geq 0 \quad \text{and} \quad \rho + p \geq 0, \quad (29)$$

the strong energy condition

$$\rho - \tau + 2p \geq 0, \qquad \rho - \tau \geq 0 \quad \text{and} \quad \rho + p \geq 0, \quad (30)$$

and the dominant energy condition

$$\rho \geq 0, \qquad \tau \in [-\rho, \rho] \quad \text{and} \quad p \in [-\rho, \rho]. \quad (31)$$

In order to probe where the bounded EBWH violates some energy conditions, we investigate where the energy density and $(\rho \mp \tau)$ and $(\rho \pm p)$ are greater than zero. In Fig. 6 we exhibit the behavior of the energy density (19) for some bounded EBWHs. We note that unlike in the unbounded case, where the energy density is nonpositive everywhere, in the internal bounded region ρ can be positive. One notes that as $x \to -\infty$, the energy density approaches a positive limit, namely $1/(8\pi R^2)$. Therefore, the smaller the asymptotic areal radius, the larger the energy density in the bounded region. In particular, if $R = 0$, the energy density exponentially diverges inside the bounded EBWH.

The behaviors of $(\rho \pm \tau)$ and $(\rho \pm p)$ are plotted in Fig. 7. A careful look at that figure reveals that the energy conditions are satisfied in certain internal regions of the bounded universe. Near the throat they are violated, as ρ, $\rho - \tau$ and $\rho - p$ are negative; however delving into the internal region, the energy conditions are satisfied, since there is a region where ρ, $(\rho \pm \tau)$, and $(\rho \pm p)$ are positive. Such a region is followed by a small domain of energy violation and, since $\rho - \tau$ is either negative or zero, depending on the vanishing of R as $x \to -\infty$, the asymptotic bounded region can either violate or satisfy all the energy conditions. Specifically, if $R \neq 0$, it follows that $\rho - \tau \to 0$ as $x \to -\infty$. On the other hand, if $R = 0$,

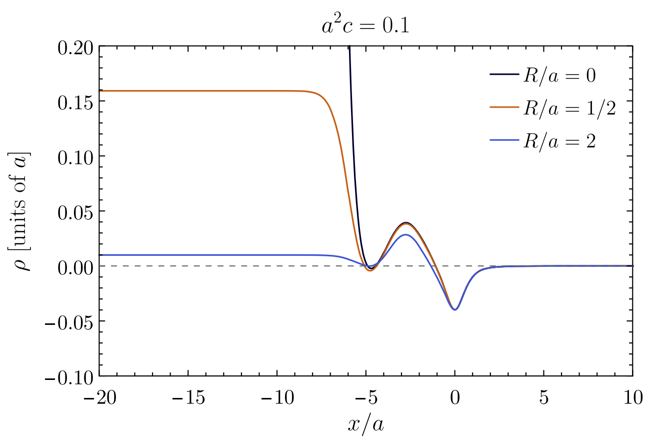

FIG. 6. Energy density of some bounded EBWHs with different asymptotic radius.

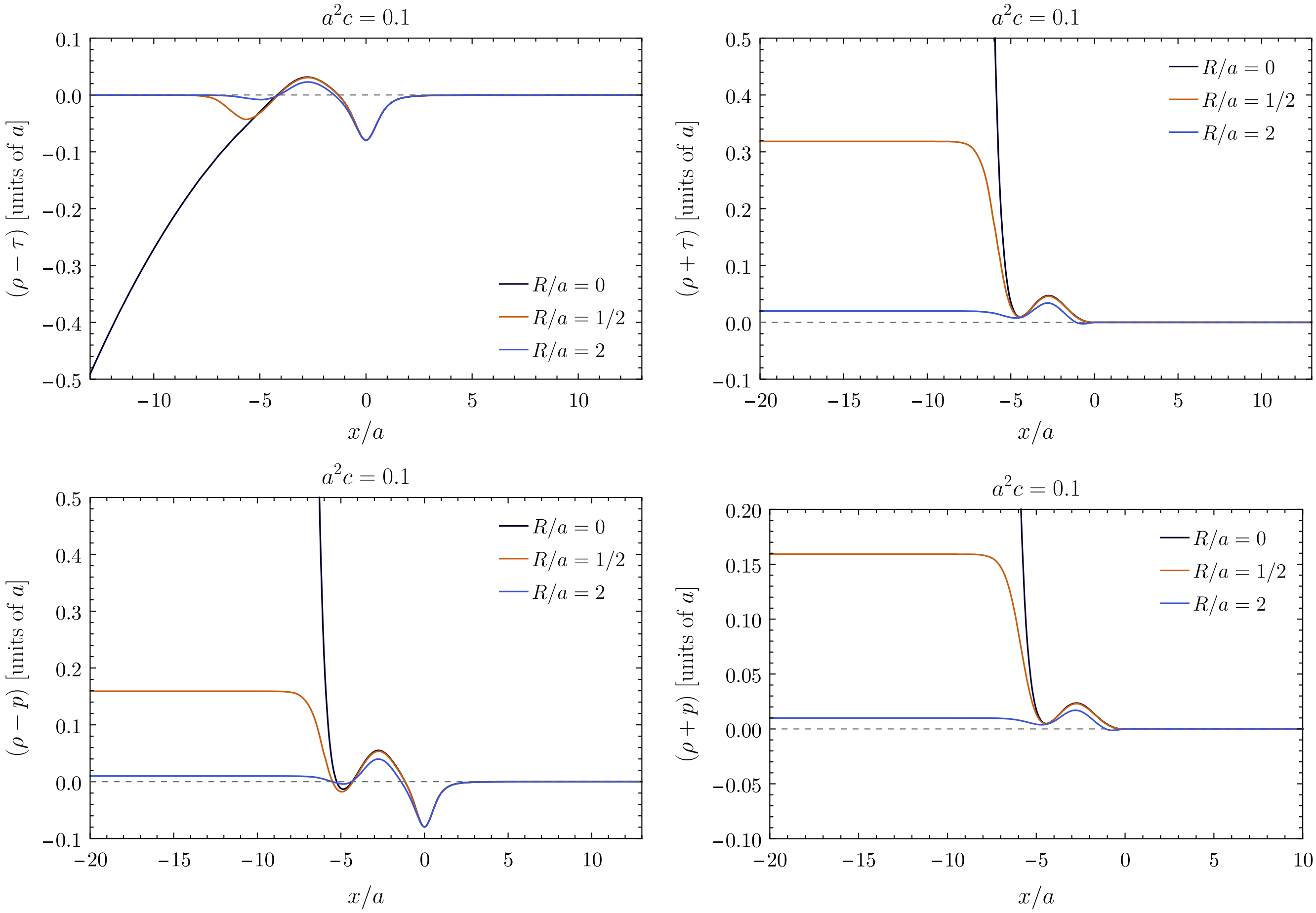

FIG. 7. Behavior of $(\rho \mp \tau)$ and $(\rho \pm p)$ in the bounded universe. The negative regions represent energy violation regions in the bounded universe.

$\rho_0 - \tau_0 \approx -c^2x^2/\pi$ as $x \to -\infty$, and thus $\rho - \tau$ is a monotonically decreasing parabola in the asymptotic internal region (cf. Fig. 7).

III. GEODESIC ANALYSIS

In this section we examine in some detail the geodesic trajectories of free point-like particles in their motion over the two regions of the modified EBWH. The geodesic equation is obtained from the Lagrangian $\mathcal{L} = \dot{s}^2/2 = k/2$, where the overdot denotes a derivative with respect to an affine parameter λ and k is the normalization of the four-velocity ($k = -1$, 0 for massive particles and light rays, respectively). Due to the symmetries of the Lagrangian, two quantities are conserved along the geodesics, namely E and L, respectively related with the time translation symmetry (the Lagrangian is independent of t) and with the rotational symmetry (the Lagrangian is independent of φ). Therefore, in the equatorial plane the geodesic equation reads

$$\dot{x}^2 = E^2 - (V_{\text{eff}} - k), \tag{32}$$

where $V_{\text{eff}} = L^2/r^2(x)$ is the so-called effective potential. By conducting a thorough analysis of (32) together with the radial function (4), we can unveil the underlying geodesic structure of the models we propose.

Let us first investigate the geodesic completeness of the modified EBWHs by considering radial geodesics ($L = 0$) moving towards the bounded internal region, which are given by

$$\dot{x}^2 = E^2 + k, \tag{33}$$

$$\dot{r}^2 = r_x^2(E^2 + k), \tag{34}$$

regardless of the asymptotic internal 2-sphere radius R. Upon integration of (33), one obtains the trajectory for outgoing particles that cross the throat into the inner region $x(\lambda) = -\sqrt{(E^2 + k)}\lambda + x_0$, where x_0 is an integration constant. Therefore, one notices that radial geodesics can extend indefinitely, regardless of the asymptotic 2-sphere radius. This is particularly relevant when the inner radius R shrinks to zero and the bounded region has a finite volume. In this case, the curvature scalars, energy density, and pressures diverge as $x \to -\infty$. However, since it takes an infinite affine time λ to reach the asymptotic infinity, the region with ill-defined properties is actually inaccessible for massive or massless particles in radial motion. From Eq. (34), one notices that the areal velocity $\dot{r}$ of particles in radial motion goes to zero when $\lambda \to \infty$ (particles going to $x \to -\infty$).

The analysis for nonradial geodesics is more involved, since we cannot obtain an analytical expression for the geodesics. However, some approximations and numerical analysis lead to interesting conclusions. First, let us consider that the asymptotic radius R is finite and nonvanishing. When this happens, as one approaches the asymptotic internal region, $\dot{x}^2$ is approximately

$$\dot{x}^2 \approx E^2 - \left(\frac{L^2}{R^2} - k\right), \tag{35}$$

which can also be integrated leading to the conclusion that even nonradial geodesics are complete for both massive and massless particles moving in the internal region of the modified EBWH with $R \neq 0$.

When $R = 0$ an interesting feature happens. In the internal region, the effective potential grows without bound and, far from the throat, it can be approximated by

$$V_{\text{eff}} \approx \frac{L^2}{4x^2} e^{2cx^2}. \tag{36}$$

This implies that any particle with nonzero angular momentum (and finite energy) must suffer a bounce in the internal region, being reflected back to the outer universe. The only particle capable of propagating indefinitely within this geometry is one with zero angular momentum, regardless of its mass, exhibiting purely radial motion. Hence, even in the vanishing R case, all geodesics are complete and one must regard such spacetime as nonsingular.

A. Stability of circular orbits and light rings

An important point to investigate is if the bounded EBWH can support stable circular orbits. This analysis can be done through the study of the Lyapunov exponents, that in a (classical) phase space, give a measure of the average rate at which two nearby trajectories converge (or diverge).

Let us briefly review the Lyapunov exponent technique and how to obtain them by the matrix method [57–59]. In order to determine the Lyapunov exponent, we begin with the equations of motion of a particle, which in terms of the phase space variables, X_i, read

$$\frac{dX_i(t)}{dt} = F_i(X_j). \tag{37}$$

One can linearize the equations of motion at a certain orbit, namely

$$\frac{d\delta X_i(t)}{dt} = K_{ij}(t)\delta X_j(t), \tag{38}$$

where $K_{ij}(t)$ is the linear stability matrix defined by

$$K_{ij}(t) = \left.\frac{\partial F_i}{\partial X_j}\right|_{X_i(t)}. \tag{39}$$

One can write the solutions of Eq. (38) in terms of the evolution matrix, $L_{ij}(t)$, namely

$$\delta X_i(t) = L_{ij}(t)\delta X_j(0), \tag{40}$$

where the evolution matrix obeys $dL_{ij}(t)/dt = K_{im}L_{mj}(t)$, with $L_{ij}(0) = \delta_{ij}$. The eigenvalues of the evolution matrix lead to the principal Lyapunov exponent, namely

$$\lambda = \lim_{t\to\infty} \frac{1}{t}\left(\frac{L_{jj}(t)}{L_{jj}(0)}\right). \tag{41}$$

Such an exponent can be conveniently expressed by determining the eigenvalues of the stability matrix.

Now, the Lagrangian for a test particle in the equatorial plane of the bounded universe can be written as

$$\mathcal{L} = \frac{1}{2}\left(-\dot{t}^2 + \dot{x}^2 + r^2(x)\dot{\varphi}^2\right). \tag{42}$$

The canonical momenta derived from the above Lagrangian are $p_\mu = \partial\mathcal{L}/\partial\dot{x}^\mu$, namely

$$p_t = -\dot{t} = -E, \tag{43}$$

$$p_x = \dot{x}, \tag{44}$$

$$p_\varphi = \frac{\dot{\varphi}}{r^2(x)} = L, \tag{45}$$

where E and L are the above-mentioned energy and angular momentum of the particle conserved along the trajectory, respectively. From a Legendre transform, one writes the Hamiltonian

$$\begin{aligned}\mathcal{H} &= \dot{x}^\mu p_\mu - \mathcal{L}\\ &= \frac{1}{2}\left[-p_t^2 + p_x^2 + \frac{p_\varphi^2}{r^2(x)}\right].\end{aligned}$$

Hence the Hamilton equations, namely $\dot{x}^\mu = \partial\mathcal{H}/\partial p_\mu$ and $\dot{x}^\mu = -\partial\mathcal{H}/\partial x_\mu$, yield the equations of motion, which in the equatorial plane read

$$\dot{t} = -p_t, \qquad \dot{p}_t = 0, \tag{46}$$

$$\dot{x} = p_x, \qquad \dot{p}_x = \frac{p_\varphi^2 r'(x)}{r^3(x)}, \tag{47}$$

$$\dot{\varphi} = \frac{p_\varphi}{r^2(x)}, \qquad \dot{p}_\varphi = 0. \tag{48}$$

Moreover, recalling that $g_{\mu\nu}\dot{x}^\mu \dot{x}^\nu = k$, where $k = -1$ for massive particles and $k = 0$ for massless particles, one obtains

$$p_t = -\frac{\sqrt{p_\varphi^2 + r^2(x) + p_x^2 r^2(x)}}{r(x)} \tag{49}$$

for massive particles, and

$$p_t = -\frac{\sqrt{p_\varphi^2 + p_x^2 r^2(x)}}{r(x)} \tag{50}$$

in the massless case.

By restricting the analysis to problems that have a two-dimensional phase space, $X_i(t) = (p_x, x)$, and linearizing the system about an equilibrium circular orbit, namely by constraining

$$p_x = \sqrt{E^2 + k - \frac{L^2}{r^2(x)}} = 0, \qquad \dot{p}_x = \frac{p_\varphi^2 r'(x)}{r^3(x)} = 0, \tag{51}$$

the components of the linear stability matrix reduce to

$$K_{11} = 0, \qquad K_{21} = -\frac{p_\phi^2 r''(x)}{p_t r^3(x)},$$
$$K_{12} = -\frac{1}{p_t}, \qquad K_{22} = 0. \tag{52}$$

For such circular geodesics, the principal Lyapunov exponent can be expressed as

$$\lambda = \pm\sqrt{K_{12}K_{21}}, \tag{53}$$

where from now on we choose the positive sign. Specifically, for massless particles the principal Lyapunov exponent reads

$$\lambda_{nc} = \sqrt{\frac{r''(x)}{r(x)}}, \tag{54}$$

while for massive particles it reads

$$\lambda_{tc} = \frac{L}{\sqrt{L^2 + r^2(x)}}\sqrt{\frac{r''(x)}{r(x)}}. \tag{55}$$

It is important to point out that Lyapunov exponents are not invariant under changes of the time parametrization used. However, the ratio between the Lyapunov time scale ($\tau_\lambda = 1/\lambda$) and a relevant time scale is invariant. By introducing the orbital time scale $\tau_\Omega = 2\pi/\Omega$, one can define a critical exponent

$$\gamma = \frac{\tau_\Omega}{\tau_\lambda} = \frac{\Omega}{2\pi\lambda}, \tag{56}$$

where the orbital angular velocity (angular frequency) is given by

$$\Omega = \frac{\dot{\varphi}}{\dot{t}}. \tag{57}$$

Then, the angular frequency for light-like circular orbits is

$$\Omega_{nc} = \frac{1}{r(x)}, \tag{58}$$

while the angular frequency for time-like circular orbits is

$$\Omega_{tc} = \frac{L}{r(x)\sqrt{L^2 + r^2(x)}}, \tag{59}$$

such that the ratio $\Omega_{tc}/\Omega_{nc} = L^2/\sqrt{L^2 + r^2(x)}$. We notice that, for both massive and massless particles, the critical exponent on circular orbits reads

$$\gamma = \frac{1}{2\pi\sqrt{r(x)r''(x)}}. \tag{60}$$

Moreover, it is convenient to introduce the dimensionless instability exponent as λ/Ω_{nc}.

Depending on the positiveness of λ^2, one determines if the circular orbit is stable, marginally stable or unstable, namely

$$\begin{cases} \lambda^2 < 0\text{: stable circular orbit;} \\ \lambda^2 = 0\text{: marginally stable circular orbit;} \\ \lambda^2 > 0\text{: unstable circular orbit.} \end{cases} \tag{61}$$

For unstable circular orbits, tiny perturbations in the circular motion lead to chaos. Also, the larger the Lyapunov exponent, the stronger the perturbation.

Hence, from the equilibrium orbits condition (51), it follows that local minima or local maxima in the areal radius are the only allowed radii that lead to circular orbits. In the unbounded case $c = 0$, the areal radius $r(x) = \sqrt{x^2 + a^2}$ presents only a local minimum at $x = 0$, which corresponds to the throat radius, $r(0) = a$. Thus, if the conserved quantities E and L satisfy

$$E^2 + k - \frac{L^2}{a^2} = 0 \tag{62}$$

the particle is at a circular orbit at $r(0) = a$. From the analysis of the Lyapunov exponent at that radius, the circular motion at the throat is unstable since $r''(0) = 1/a > 0$ and consequently $\lambda^2 > 0$.

Therefore, light-like particles ($k = 0$) are in unstable circular motion at the throat if the ratio $L/E = a$, hereafter called *unstable light rings*. The Lyapunov exponent at the throat for light-like particles is

$$\lambda_{nc} = \frac{1}{a}, \tag{63}$$

and the dimensionless instability exponent at the throat is $\lambda_{nc}/\Omega_{nc} = 1$. On the other hand, for time-like geodesics ($k = -1$) to be in an unstable circular motion at the throat, the values of the constants of motion E and L along the trajectory are such that only particles with

$$E = \sqrt{1 + \frac{L^2}{a^2}} > 1 \tag{64}$$

are in an unstable circular orbit at the throat. Therefore, the bigger the angular momentum of the particle, the bigger should its energy be in order to guarantee the circular motion at the throat. The Lyapunov exponent at the throat for time-like particles is

$$\lambda_{tc} = \frac{L}{a\sqrt{L^2 + a^2}}, \tag{65}$$

and the dimensionless instability exponent at the throat is $\lambda_{tc}/\Omega_{nc} = L/\sqrt{L^2 + a^2}$. One thus concludes that in the EBWH there are no stable circular orbits outside the throat, and that the only allowed circular orbits are unstable ones located at the throat. As a consequence, there is no innermost stable circular orbit in this spacetime, which implies that no accretion disks can develop in such a scenario [60].

A bounded internal region inside the throat sharply modifies the geodesic structure of the spacetime. The areal radius of the bounded universe may present additional extrema in the inner region of the spacetime. For instance, depending on the model parameters, there is a local maximum of $r(x)$ at $x = x_m < 0$, where $r'(x_m) = 0$ and $r''(x_m) < 0$. Such a radius corresponds to a circular orbit if along the geodesic the constants of motion satisfy

$$E^2 + k - \frac{L^2}{r_m^2} = 0, \tag{66}$$

where $r(x_m) = r_m$. From the analysis of the Lyapunov exponent at that radius, it follows that the circular motion at r_m is stable since $r''(x_m) < 0$ and consequently $\lambda^2 < 0$.

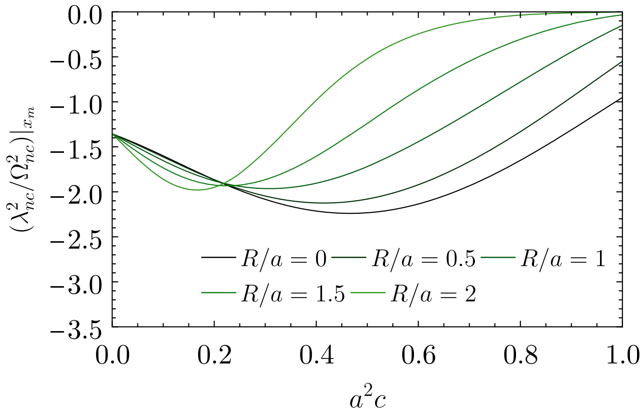

FIG. 8. Behavior of the dimensionless ratio $\lambda_{nc}^2/\Omega_{nc}^2$ at the stable circular orbit inside the bounded universe. We note that $\lambda_{nc}^2/\Omega_{nc}^2$ has a minimum for some value of c. Additionally, that quantity approaches zero as c increases, indicating that the stable circular orbit degenerates in the marginal circular orbit in the asymptotic region.

Therefore, photons with $L/E = r_m$ at r_m are in stable circular orbits. Those orbits are called *stable light rings*. The Lyapunov exponent at the stable light ring is

$$\lambda_{nc} = \sqrt{\frac{r''(x_m)}{r_m}}, \tag{67}$$

which in general has dependences on a, c, and R. The dimensionless instability exponent at the stable light ring is $\lambda_{nc}/\Omega_{nc} = \sqrt{r_m r''(x_m)}$. We show the negativeness of the dimensionless quantity $\lambda_{nc}^2/\Omega_{nc}^2$ at r_m in Fig. 8. We point out that the existence of stable light rings may support long-lived modes (radiation may be trapped by these compact objects). In Sec. IV we discuss trapped scalar modes.

Remarkably, unlike in the unbounded case, the internal region of the bounded universe can support massive particles in stable circular orbits. At r_m, time-like geodesics with energy

$$E = \sqrt{1 + \frac{L^2}{r_m^2}} > 1 \tag{68}$$

are allowed to stay in a stable circular orbit at r_m. The energy of such particles should be bigger as the angular momentum of the particle is bigger. We note that, since $r_m > a$ (recall that r_m is a local maximum while a is a local minimum), time-like geodesics at stable circular orbits demand less energetic particles than time-like geodesics at unstable circular orbits. The Lyapunov exponent at r_m for time-like particles is

$$\lambda_{tc} = \frac{L}{\sqrt{L^2 + r_m^2}} \sqrt{\frac{r''(x_m)}{r_m}}. \tag{69}$$

Performing a similar analysis in the asymptotic internal region of bounded universes shows that as $x \to -\infty$, particles with nonzero angular momentum approach a circular motion with radius R. In the bounded universe with radius $R \neq 0$, the asymptotic value of the canonical momentum p_x is

$$\lim_{x\to-\infty} p_x = \sqrt{E^2 + k - \frac{L^2}{R^2}}, \tag{70}$$

while its derivative, $\dot{p}_x$, vanishes asymptotically since $r'(x)$ vanishes as $x \to -\infty$, namely

$$\lim_{x\to-\infty} \dot{p}_x = \lim_{x\to-\infty} \frac{L^2 r'(x)}{r^3(x)} = 0. \tag{71}$$

Then, asymptotically, photons with $L/E = R$ approach a circular motion with radius R. Such an *asymptotic circular orbit* has a vanishing Lyapunov exponent, namely

$$\lim_{x\to-\infty} \lambda_{nc} = \lim_{x\to-\infty} \sqrt{\frac{r''(x)}{r(x)}} = 0. \tag{72}$$

Therefore that asymptotic orbit is marginally stable. Hence, the asymptotic region of the bounded universe possesses a *marginally stable light ring*. Moreover, asymptotically, massive particles also approach a circular motion as $x \to -\infty$ if their energy satisfies

$$E = \sqrt{1 + \frac{L^2}{R^2}} > 1. \tag{73}$$

The Lyapunov exponent of that time-like asymptotically circular orbit vanishes as well, namely

$$\lim_{x\to-\infty} \lambda_{tc} = \lim_{x\to-\infty} \frac{L}{\sqrt{L^2 + r^2(x)}} \sqrt{\frac{r''(x)}{r(x)}} = 0, \tag{74}$$

which tells us that such orbits are also marginally stable. One notices that the dimensionless instability factor in those cases vanishes regardless of the asymptotic value R. The asymptotic boundedness of the universe induces marginal stability of time-like and null-like orbits. We remark that, if the areal radius $r(x)$ shrinks to zero as $x \to -\infty$ ($R = 0$), no circular orbit exists in the asymptotic region of the bounded universe.

B. Photon orbits

To better understand the geodesic structure of the modified EBWH, one can analyze general orbits within these geometries. Here, for simplicity, we specifically focus on null orbits ($k = 0$), so that Eq. (32) can be rewritten as

$$\frac{1}{r^4}\left(\frac{dx}{d\varphi}\right)^2 = \frac{1}{b^2} - \tilde{V}_{\rm eff}(x), \tag{75}$$

where $b = L/E$ is the so-called impact parameter and $\tilde{V}_{\rm eff}(x) \equiv V_{\rm eff}(x)/L^2 = 1/r^2(x)$.

First, let us consider null geodesics impinging on the modified EBWH from the outer universe. As we saw, there is an unstable photon sphere at the throat of our model. Thus, photons impinging from the outer universe with impact parameter greater than the throat radius, $b > a$, do not enter the inner universe and are scattered back to infinity, while photons with impact parameters smaller than the throat radius, $b < a$, do cross the throat and enter the inner universe. Photons with impact parameter equal to the throat radius, $b = a$, stay trapped in the unstable photon sphere. In the unbounded EBWH scenario, photons that cross the throat never come back to the outer universe. However, as discussed above, in bounded models, there are geodesics that upon crossing the throat are allowed to return to the outer universe.

Such bouncing behavior can be visualized from the analysis of the effective potential $\tilde{V}_{\rm eff}$. In Fig. 9 we show the effective potential of some configurations of bounded EBWH, together with the inverse of the impact parameter squared of some photons able to cross the throat (horizontal lines). The point where a horizontal line meets the effective potential, say x_b, characterizes a turning point, where the photon suffers a bounce (i.e. the photon is reflected in the inner universe). For a nonvanishing asymptotic 2-sphere radius, the potential goes to a barrier of magnitude $1/R^2$ as $x \to -\infty$, while for $R = 0$, the effective potential

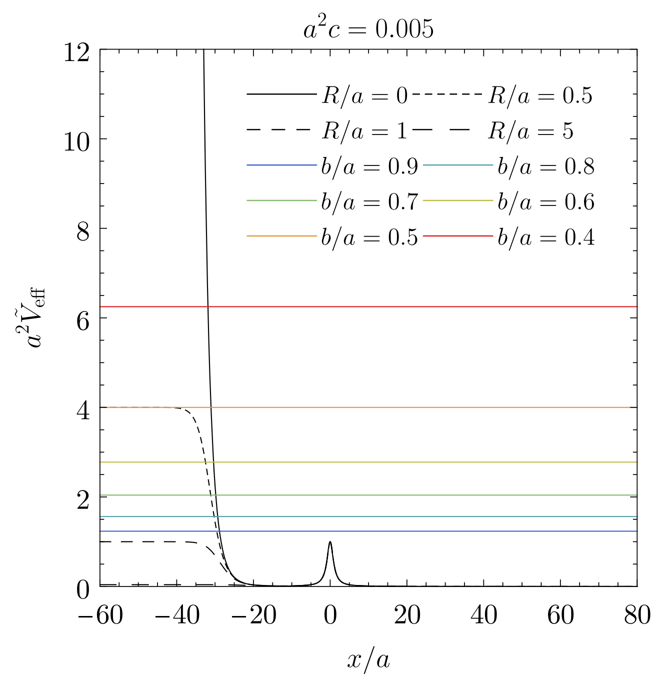

FIG. 9. Effective potential of four modified EBWHs with fixed c and four choices of R, namely $R/a = 0$, 0.5, 1 and 5. We also plot the inverse of the impact parameter squared of some photons that enter the inner region of the modified EBWH.

exponentially grows inside the throat [cf. Eq. (36)]. Any photon able to enter the inner universe ($b < a$), propagates into a bounded 2-sphere universe, and the behavior of its trajectory depends on the asymptotic radius R. For $R \geq a$, photons crossing the throat must propagate towards asymptotic infinity, since the asymptotic value of the effective potential $1/R^2 \leq 1/a^2$. However for $R < a$, after crossing the throat, depending on their impact parameter, photons may suffer a bounce in the inner universe, since $1/R^2 > 1/a^2$. Specifically, for nonradial geodesics ($L \neq 0$), the bounce happens if given an impact parameter b, there is an $x = x_b$ such that $\tilde{V}_{\rm eff}(x_b) = 1/b^2$ and $\tilde{V}_{\rm eff} > 1/b^2$ for $x < x_b$. At x_b therefore a bounce happens and the particle is scattered to the outer universe.

In Fig. 10 we show how the four configurations shown in Fig. 9 scatter light rays with the same impact parameter in

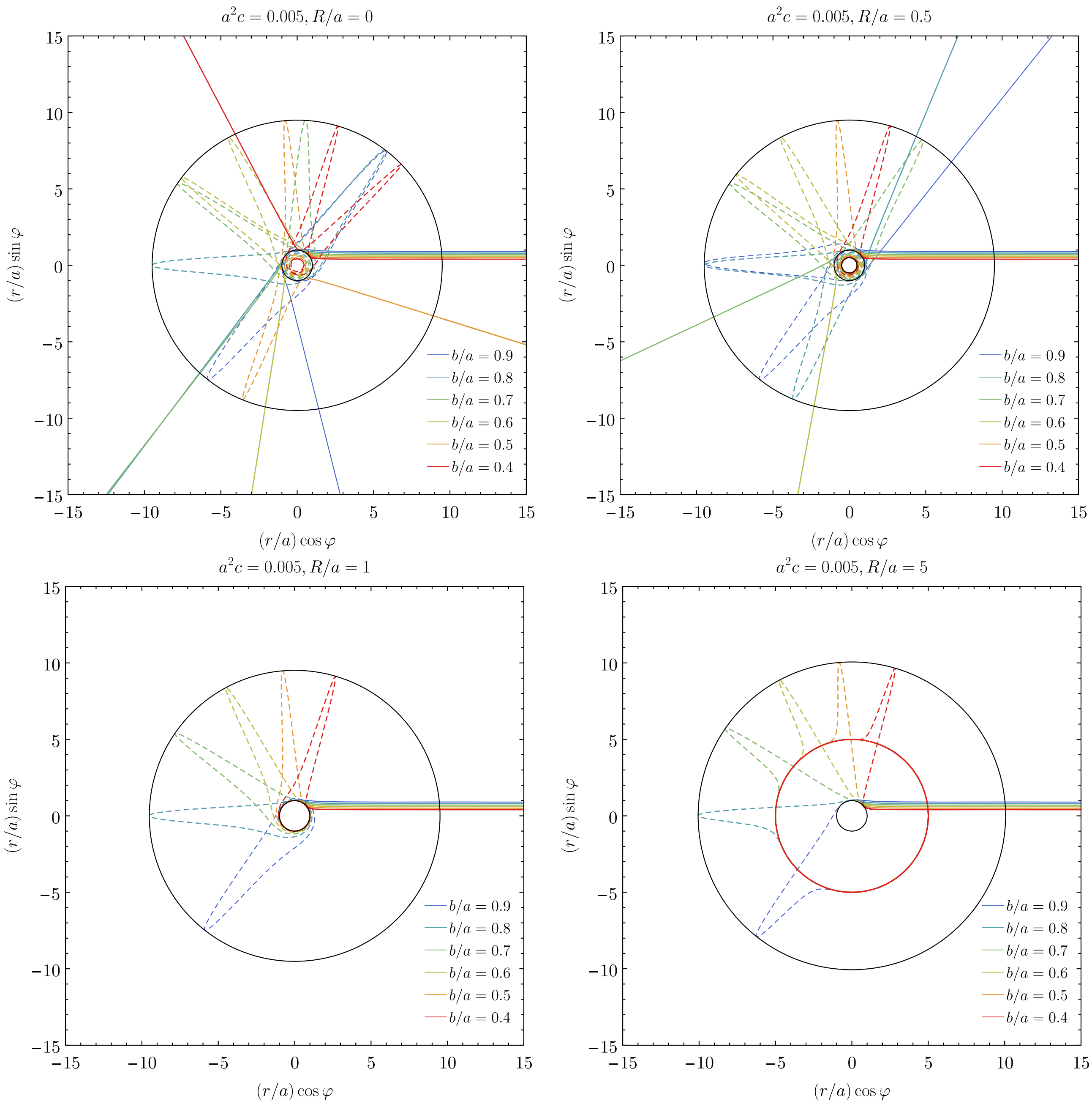

FIG. 10. Null geodesics in the modified EBWH. Solid lines correspond to light rays propagating in the outer universe, while dashed lines represent geodesics in the inner universe. We consider photons with the same values of impact parameter in the outer universe, and show how these photons are scattered or absorbed depending on the modified EBWH configuration. The circle with radius 1 corresponds to the throat of the wormhole; the outermost circle corresponds to the local maximum of the areal radius $r(x)$ in the inner universe. The other circles are the asymptotic 2-sphere radius of each configuration.

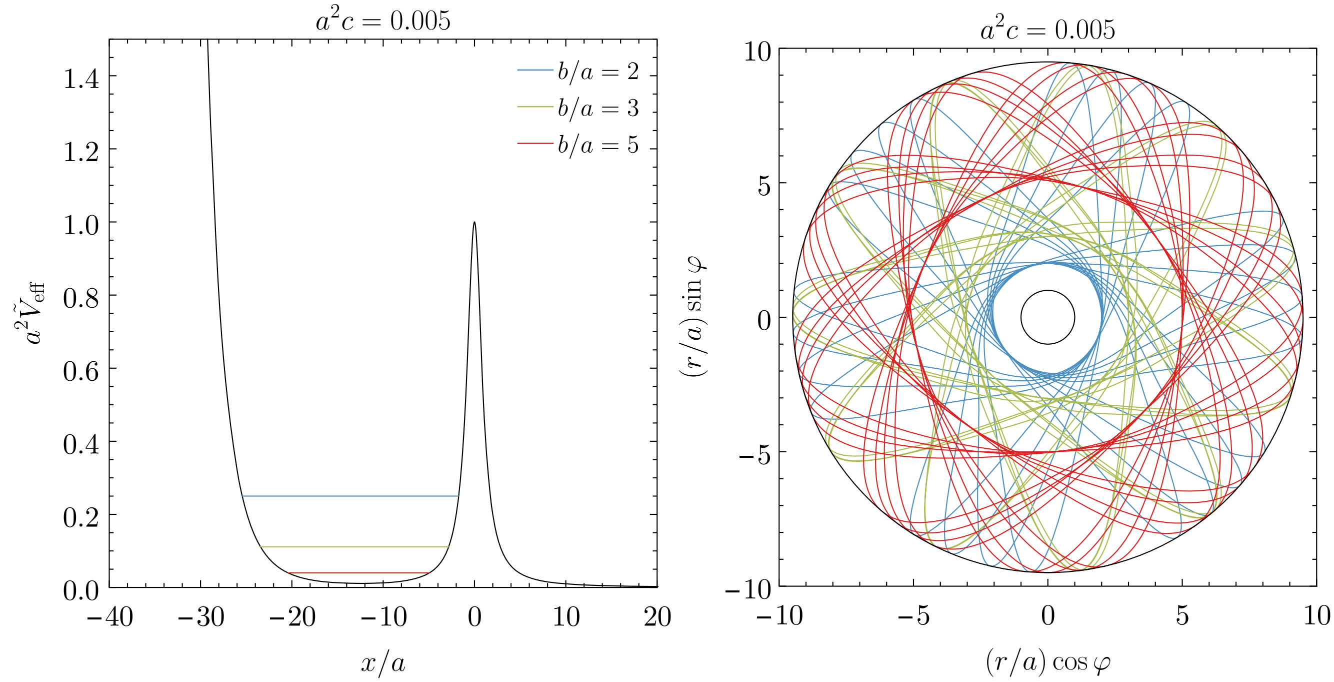

FIG. 11. Trapped null geodesics inside a finite-volume bounded EBWH ($R = 0$). Initially, the geodesics are at their corresponding inner turning point, x_b, and are evolved from an initial angle $\varphi_0 = 0$ to an angle $\varphi_f = 200$. The inner and outer black circles denote the local minimum and the local maximum of the bounded EBWH, respectively.

the outer universe. In the top-left panel, the geodesics propagate in the modified EBWH with vanishing asymptotic 2-sphere radius. As previously discussed, any nonradial geodesic moving through the inner region must suffer a bounce. This behavior is shown in the top-left panel of Fig. 10. When $R < a$, depending on the impact parameter the geodesic can be scattered to the outer universe or propagate to the asymptotic internal region. We exhibit this behavior in the top-right panel of Fig. 10. We can see that, geodesics with impact parameter $b \le R$ are scattered back to the outer universe, and any other geodesic crossing the throat must propagate to the asymptotic internal region with a bounded 2-sphere. The bottom-left and bottom-right panels, respectively, exhibit geodesics in $R = a$ and $R > a$ modified EBWHs. In these configurations any photon crossing the throat to the inner universe, propagates toward it to the asymptotic internal region with a bounded 2-sphere.

As previously discussed, the geodesic structure of the internal region is richer than the outer one, and stable light rings may be present. When they exist, the effective potential exhibits a well, and families of trapped geodesics are allowed to stay inside the bounded universe. For this to happen, the photon energy and angular momentum must be such that $1/b^2 = E^2/L^2$ is smaller than the potential barrier at the throat $(1/a^2)$ and than the asymptotic value of $\tilde{V}_{\text{eff}}$ in the internal region. The trapped orbits represent an oscillatory motion between these two turning points inside the well. To illustrate this behavior, in the left panel of Fig. 11 we show, as horizontal lines, the ratio $1/b^2 = E^2/L^2$ of three trapped orbits inside a finite-volume bounded universe. The values of x where the horizontal lines have the same value as the effective potential are the turning points of the trapped orbits. In the right panel of Fig. 11, we represent these orbits confined within the bounded region. Note that photons with smaller $1/b^2$ oscillate between nearer turning points, which is translated into the trapped orbit being more concentrated near the stable light ring (the local maximum of the bounded region).

It is important to point out that the potential well is formed, in general, by two potential barriers with different heights (cf. Fig. 9). Specifically, if $R > a$ the higher barrier is the one at the throat, while if $R < a$, the higher barrier is the one associated with the bounded 2-sphere core. Hence, the smaller the asymptotic 2-sphere radius, the greater the ratio E/L one can find in photons at trapped orbits. Since photons with ratio $E/L > 1$ can escape from the bounded region, photons at trapped orbits cannot have such a ratio. Therefore, in a bounded EBWH with $R < a$, there are photons with ratio $1/x_m \le E/L < 1/a$ at trapped orbits within the bounded region, whereas, if $R > a$, one can only find photons with ratio $1/x_m \le E/L < 1/R$ at trapped orbits within the bounded region. We remark that, photons with $E/L = 1/x_m$ at trapped orbits within the bounded universe are the ones at the stable light ring.

IV. SCALAR FIELD PERTURBATIONS

In order to extract valuable information about the geometries investigated in this study, we turn our attention to the analysis of scalar perturbations on the background metric $g_{\mu\nu}$. By examining the evolution of these perturbations, we can discern the distinctive effects that these geometries imprint on the time-domain profiles, making them distinguishable from other black hole and wormhole configurations.

For a massless scalar field Ψ localized within the background metric $g_{\mu\nu}$, the dynamics of the field are governed by the Klein-Gordon equation

$$\Box\Psi(t,x,\theta,\varphi) = 0. \tag{76}$$

Due to the spherical symmetry of the problem, we can decompose the field in the following way:

$$\Psi(x^\mu) = \sum_{\ell=0}^{\infty}\sum_{m=-\ell}^{\ell}\frac{\Phi(x,t)}{r(x)}Y_{\ell m}(\theta,\varphi), \tag{77}$$

where $Y_{\ell m}(\theta,\varphi)$ denotes spherical harmonics of degree ℓ and order m. By substituting (77) into (76), one obtains that the radial function $\Phi(x,t)$ must satisfy

$$\left(\frac{d^2}{dt^2} - \frac{d^2}{dx^2} + V_\Phi\right)\Phi = 0, \tag{78}$$

where the effective potential V_Φ is given by

$$V_\Phi = \frac{\ell(\ell+1)}{r^2(x)} + \frac{r_{xx}}{r(x)}. \tag{79}$$

Now, in order to integrate the wave equation (78) we follow the procedure described in [61]. This involves introducing light-cone coordinates, specifically the advanced time coordinate denoted as $v \equiv t + x$ and the retarded time coordinate denoted as $u \equiv t - x$. Thus, the wave equation can be expressed as

$$\left(4\frac{d^2}{du dv} + V_\Phi\right)\Phi = 0. \tag{80}$$

The integration of this differential equation is done numerically on a null grid which leads to the following expression for the discretized scalar field evolution:

$$\Phi_N = \Phi_E + \Phi_W - \Phi_S - \frac{h^2}{8}V_\Phi(S)(\Phi_W + \Phi_E) + O(h^4), \tag{81}$$

where h is the step size between two neighboring grid points and subscripts indicate the point in the grid where the function is evaluated. Explicitly, $S = (u, v)$, $W = (u + h, v)$, $E = (u, v + h)$ and $N = (u + h, v + h)$, as can be seen more clearly in Fig. 12.

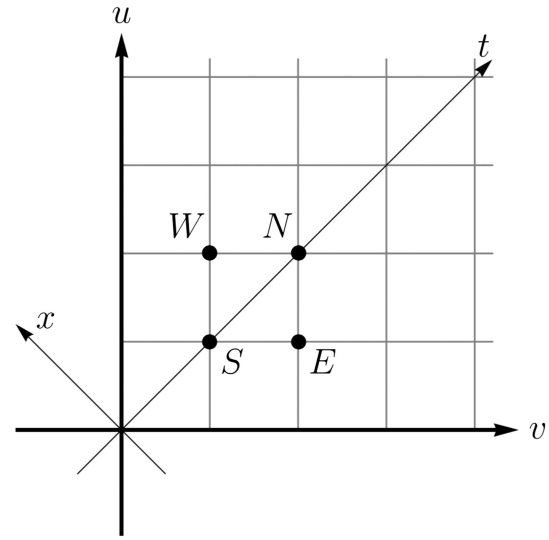

FIG. 12. Representation of the numerical grid used for the integration of (80). The evaluation points of (81) are represented with S, W, E and N. The step size of the grid can be visualized by the distance between two consecutive points on the same axis $h = u_E - u_S = v_N - v_E$.

The initial distribution for the scalar perturbation is set on the null surfaces $u = 0$ and $v = 0$. Then, the grid is computed line by line using the mechanism described in (81), with a step size $h = 0.1$ and grid values ranging from $u_{\min} = 0$ to $u_{\max} = 1000$ and $v_{\min} = 0$ to $v_{\max} = 1000$. As initial conditions for the scalar perturbation we use a Gaussian distribution on the $u = 0$ surface, together with a constant profile on the $v = 0$ surface, i.e.

$$\Phi(0, v) = Ae^{-(v-v_c)^2/2\sigma^2}, \tag{82}$$

with height $A = 1$, width $\sigma^2 = 4.5$ and centered at $v_c = 20$.

The effective potential is then calculated by applying (79) and using the radial function $r(x)$ as presented in (4). Radial profiles of the effective potential with $R/a = 0$ are depicted in Fig. 13 where, in order to optimize the designed grid, the throat of the wormhole has been conveniently shifted to $x = -20$ in our numerical computations. Once we have obtained our numerical data, we will restore the throat position to $x = 0$ to align our analysis more closely to the rest of the paper. As one can see, the effective potential exhibits a peak like in standard EBWHs, which is associated to the throat of the wormhole, and with their maximum value increasing in proportion to ℓ. Conversely, as x tends to $-\infty$, the potential does not drop to zero, but it shows a rapid and smooth growth, remaining finite for all finite radial values. It is remarkable that the effective potential exhibits a significantly slower growth as x approaches $-\infty$ for the fundamental ℓ mode as compared to higher ℓ modes. Moreover, with increasing values of ℓ,

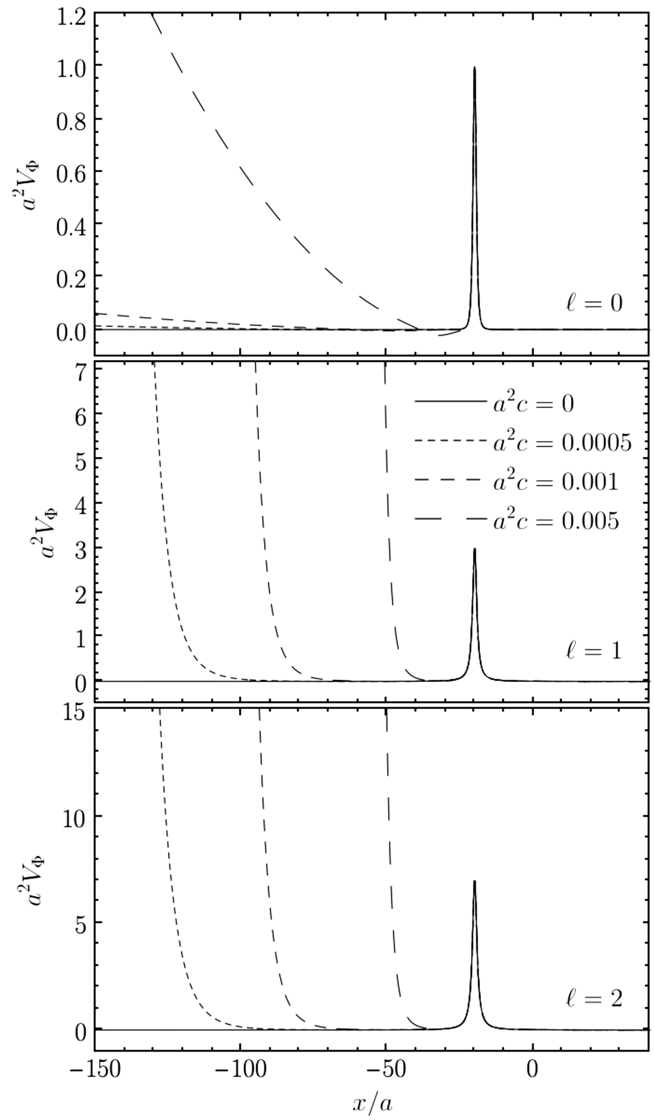

FIG. 13. The radial profiles of the effective potential (79) are presented for three ℓ modes and $R/a = 0$. The top panel displays the case for $\ell = 0$, the central panel shows $\ell = 1$, and the bottom panel shows $\ell = 2$. The solid line represents the radial profile of the effective potential for the standard EBWH, while dashed lines correspond to three different configurations of modified EBWH with varying c parameters.

it approaches infinity at a faster rate, although the most prominent discrepancy in growth rate is observed between $\ell = 0$ and $\ell = 1$. This can be understood by computing the leading term of the fundamental mode as $x \to -\infty$, where we notice that it behaves as $V_\Phi \approx 4c^2x^2$. This clearly has a growth rate slower than the one experienced when $\ell \neq 0$, which diverges exponentially as $V_\Phi \approx \ell(\ell+1)e^{2cx^2}/(4x^2)$. Therefore, even though the effective potential for $\ell = 2$ diverges faster than the effective potential for $\ell = 1$, they both do it exponentially. By contrast, the divergence is polynomial for the $\ell = 0$ mode. The unbounded behavior of the effective potential as $x \to -\infty$, combined with the first peak, gives rise to a well, which is expected to lead to echoes in the time-domain spectrum (see discussion in the next section). We point out that for the fundamental ℓ mode, the effective potential assumes negative values within the well near the peak associated with the throat of the wormhole. The radial extent over which a negative effective potential occurs diminishes as ℓ increases. Finally, it is worth mentioning that the parameter c exerts an influence on the effective potential, causing the well formed between the throat peak and the asymptotic boundary to narrow as its value increases.

For the nonvanishing R case, one can show that the asymptotic behavior of V_Φ reads

$$\lim_{x\to+\infty} V_\Phi = 0, \tag{83}$$

$$\lim_{x\to-\infty} V_\Phi = \begin{cases} 0, & \ell = 0, \\ \frac{\ell(\ell+1)}{R^2}, & \ell \neq 0. \end{cases} \tag{84}$$

It is worth nothing that in the asymptotic internal region, whenever $\ell \neq 0$ and $R \neq 0$, the effective potential goes to a threshold value. The massless scalar field propagating in this region would behave equivalently to a scalar field with effective mass in a Minkowski background, namely

$$\left(\frac{d^2}{dt^2} - \frac{d^2}{dx^2} + \mu_e^2\right)\Phi = 0, \tag{85}$$

where $\mu_e = \sqrt{\ell(\ell+1)}/R$. This kind of effective mass in scalar field dynamics typically arises in nonasymptotically flat spacetimes, such as when scalar waves propagate around a black hole immersed in a magnetic field [62,63]. For the case $\ell = 0$, the effective potential vanishes asymptotically on both sides of the modified EBWH, and therefore no effective mass term appears.

In Fig. 14, we depict the radial profiles of the effective potential for $\ell = 1$ and various values of the R parameter. As observed in the geodesic analysis, the presence of a nonzero R leads to the asymptotic finiteness of the potential as $x \to -\infty$. The finite value towards which the potential tends is inversely proportional to the magnitude of R^2, with the potential becoming approximately 2 orders of magnitude smaller than the throat peak for $R/a = 5$.

As the 2-sphere approaches its asymptotic value, the effective potential exhibits a sort of effective centrifugal barrier for $R = 0$, playing the role of an effective mirror for the scalar field perturbation. For $R \neq 0$ in this same limit, one can see that the effective potential tends to a plateau whose height is proportional to $1/R^2$.

A. Time domain profile: Echoes

After solving the discretized wave equation, we extract the scalar field values at the observation point $x_{\text{obs}} = 0$

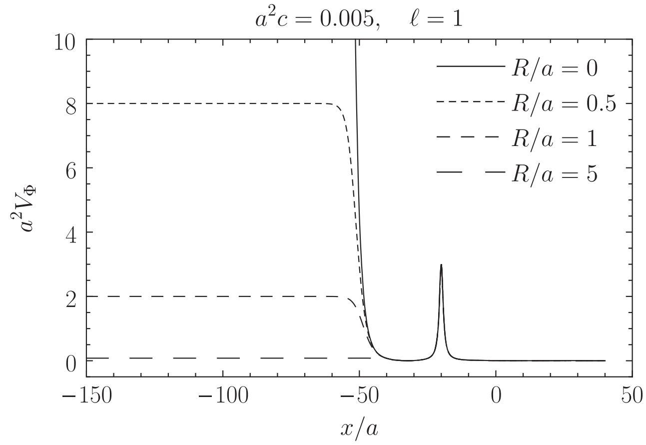

FIG. 14. The radial profiles of the effective potential (79) are presented for four configurations with different R parameter and $\ell = 1$.

using the coordinate transformation $x = (u - v)/2$ and $t = (u + v)/2$. Even though our model allows for arbitrarily large values of c, here we are focusing on small deviations of EBWHs in the throat scale, and therefore restricting our analysis to $a^2c \leq 0.005$. This results in the potential peak at the throat being almost the same as in the EBWH (see Figs. 13 and 14). As the initial wave packet impinges on the modified EBWH, it encounters the throat peak first, causing a portion of the wave to return back to the observation point exhibiting a characteristic ringdown. Due to the similarities between the throat peaks of modified and standard EBWHs, the prompt contribution and initial ringdown signal in the time profile of scalar perturbations are expected to be basically the same in both scenarios.

The portion of the scalar wave packet that is transmitted by the throat peak passes through the well and encounters the potential barrier extending to $x \to -\infty$. It then reflects back towards the observation point. However, in order to reach $x_{\rm obs}$, it must interact with the throat peak once again. A portion of the incident wave is reflected, repeating the same process, while another portion is transmitted. The transmitted portion, after being detected at the observation point, evolves towards $x \to \infty$ and does not pass through the observation point again. Each time a wave is reflected and passes through the observation point, it is recorded as a peak in the time-domain profile of $|\Phi_\ell|$. As expected based on the description of the effective potential of the modified EBWH, (unstable) photon sphere modes from the scalar perturbation exist and ring in the same way as in a standard EBWH. However, in this case, there is a stable photon sphere in the inner universe, causing the bounded 2-sphere region of the wormhole to act as a cavity, trapping photon sphere modes. This results in a series of echoes in the scalar perturbation time profile—the periodic disturbances in the late-time behavior of the scalar waveform, telling apart the ringdown profile of the bounded universe model from the unbounded EBWH one, which are illustrated in Fig. 15 for the bounded universe model with vanishing asymptotic 2-sphere radius. The characteristics of these echoes vary depending on the parameters used to construct the spacetime, since the width and height of the cavity in the effective potential deeply depend on c and R, as can be seen in Fig. 16.

First, let us discuss the $R = 0$ spacetimes in order to gain some intuition on the role of the parameter c. It can be observed that there is a relationship between the value of this parameter and the frequency of the echoes (cf. left column of Fig. 16). This arises from the fact that c influences the width of the effective potential well. As the well becomes narrower with increasing c, it can be observed that the time interval between two consecutive echoes, Δt, decreases (or, equivalently the frequency increases), as the waves have to travel a shorter distance. In order to estimate this time interval, one usually computes the time a light signal takes to return to the throat after a

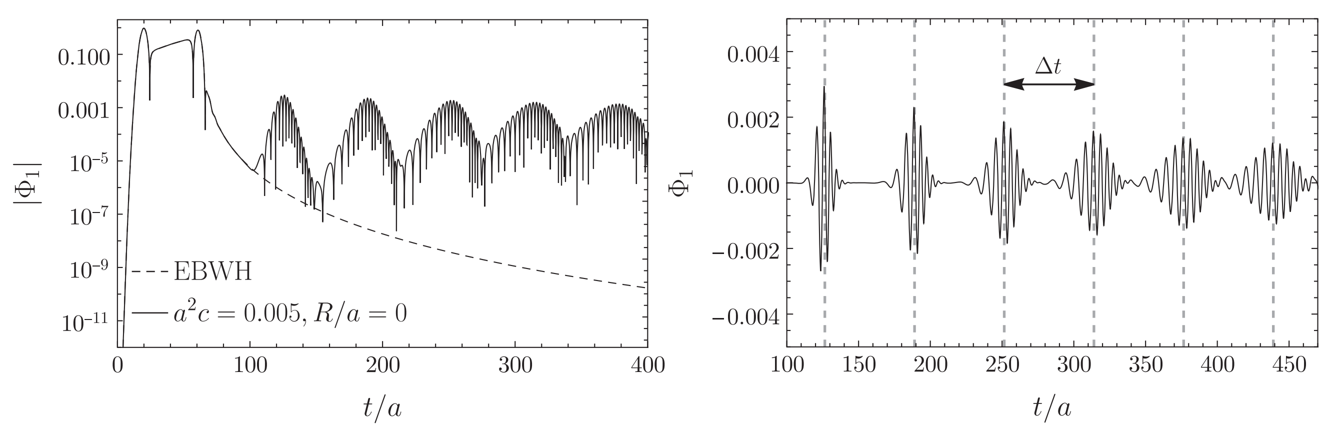

FIG. 15. Left: time-domain profile of the absolute value of the scalar field perturbation for the $\ell = 1$ mode of the EBWH and a bounded universe model with $a^2c = 0.005$ and $R/a = 0$. The disparity between the EBWH and the other cases are the so-called echoes. Right: the late-time behavior of the scalar waveform in the considered bounded universe model. For such s configuration, the time interval between two successive echoes is $\Delta t/a \approx 62$.

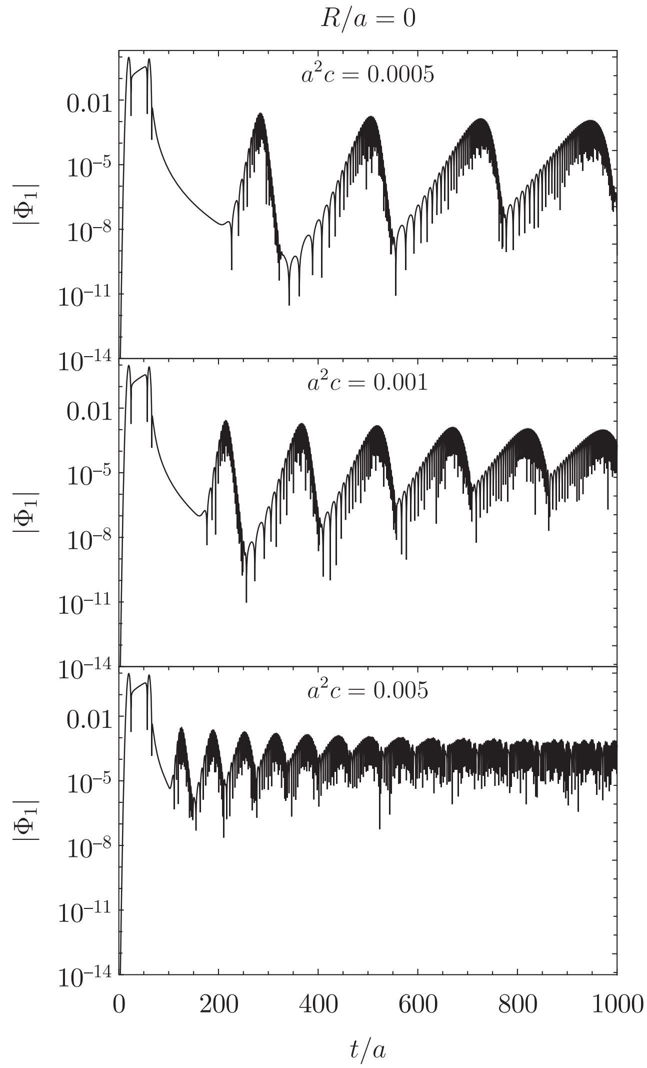

FIG. 16. Time-domain profile of the absolute value of the scalar field perturbation for the $\ell = 1$ mode for different bounded universe models. In the left column, three configurations with varying values of the parameter c and $R/a = 0$ are displayed. In the right column, three configurations with different values of the parameter c are shown, but with $R/a = 5$.

bounce in an internal potential barrier, which is roughly given by

$$\Delta t \sim 2 \int_{x_b}^{0} dx = 2|x_b|, \tag{86}$$

which depends nontrivially on the bounded universe parameter c and on the impact parameter b of the photon. In this way, the internal turning point basically acts as an effective width of the cavity. A good estimation of the time delay between consecutive echoes, therefore, deeply depends on the construction of the effective width. Remarkably, for dipolar modes ($\ell = 1$), we have found a suitable procedure for determining the effective width of the cavity. It consists of taking x_b such that $V_\Phi(x_b)$ has approximately the value of the effective potential at the throat, namely $V_\Phi(0)^2$. Since we are considering $a^2c \leq 0.005$, x_b is expected to be far from the throat, where the effective potential can be approximated, for $\ell = 1$, by $V_\Phi \approx e^{2cx^2}/(2x^2)$. Therefore, in units of a, x_b is approximately given by the (negative) root of

$$\frac{e^{2cx_b^2}}{2x_b^2} = 9. \tag{87}$$

By numerically solving this equation we find the effective width, $|x_b|$, and a good estimation for the time delay between consecutive echoes is found as $\Delta t = 2|x_b|$. Specifically, the $\ell = 1$ echoes' time delay for the configurations shown in Fig. 16, namely $a^2c = 0.0005$, $a^2c = 0.001$ and $a^2c = 0.005$, are respectively $\Delta t/a \approx 222$, $\Delta t/a \approx 152$ and $\Delta t/a \approx 62$. Hence, as we expected, increasing c leads to narrower bounded universes and implies the presence of echoes with shorter time delays.

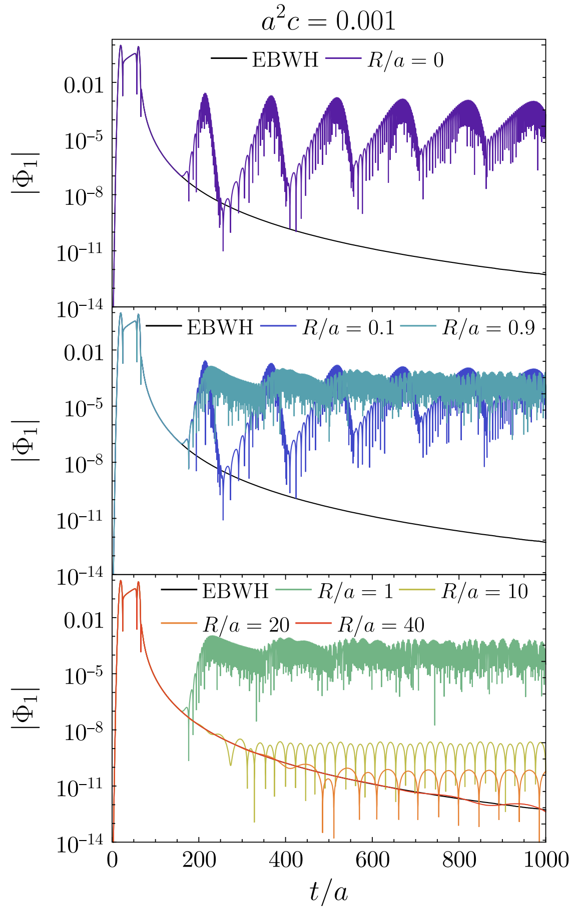

FIG. 17. Time-domain profile of the absolute value of the scalar field perturbation for the $\ell = 1$ mode. Seven configurations with the values $R/a = \{0, 0.5, 0.9, 1, 10, 20, 40\}$ are plotted, along with the EBWH as a reference.

Another notable feature that can be observed is the gradual decay of peak amplitudes. Each time the scalar wave packet interacts with the throat peak, it is divided into transmitted and reflected parts, resulting in weaker successive echoes. This effect contrasts with the case of the EBWH, where the signal exhibits a rapid decay compared to the modified EBWH scenario. The presence of two asymptotic infinities and the absence of a potential well in the EBWH prevent the emergence of echoes, thereby contributing to the faster signal decay. When the potential well is narrower, the superposition of different echoes becomes more noticeable, leading to deformations in their waveforms. This behavior is particularly evident in the late-time regime, as shown by the bottom plot in the left column of Fig. 16.

Similar features are also noticeable in the right column of Fig. 16, corresponding to the $R/a = 5$ configuration. However, the echoes' amplitudes are notably smaller compared to the previous scenario, making it difficult to differentiate distinct echoes due to their reduced amplitude.

The absence of an unbounded growing effective potential results in wave packets interacting with a finite barrier, leading once again to the division of the package into a reflected part and a transmitted part that propagates towards $x \to -\infty$ without bouncing back to the outer universe. The height of the barrier diminishes as R increases, making it evident that the reflected part of the wave is also smaller as one considers bigger values of R, as shown in Fig. 17. Notably, there is a distinct transition regime depending on the asymptotic value to which the effective potential tends. Specifically, the asymptotic value aligns with the height of the throat peak for $R/a \approx 0.8$ for the considered configurations. When the barrier exceeds the throat peak height ($R/a < 0.8$), the echoes are easily distinguishable. However, when the barrier is smaller ($R/a > 0.8$), a higher proportion of the wave is lost, leading to a reduction in the amplitude of the echoes. Remarkably, by considering $c \ll 1$, the time-domain profile of the modified EBWH with large asymptotic 2-sphere radius, tends towards the expected profile of a standard EBWH.

For late times, we observe a diminishment in the damping of the echoes of the scalar wave. At this point, so-called quasiresonances are present—arbitrarily long-lived quasinormal modes (QNMs) [64]. These modes were discussed in the QNM analysis of massive fields in asymptotically flat spacetimes [64,65], and also appear in nonasymptotically flat scenarios where the wave equation acquires a sort of effective mass [63,66]. Our model pertains to the latter case.

Finally, it is noteworthy that while the results presented here are for the $\ell = 1$ mode, the qualitative characteristics are present in the other ℓ modes as well.

V. FINAL REMARKS

We have introduced a new class of modified EBWHs, where one side of the global spacetime geometry, usually consisting in an asymptotic Minkowski region, is supplanted by a bounded 2-sphere patch, where the areal radius is finite and asymptotically constant. The resulting asymmetric wormhole is still endowed with a local minimum in the areal radius, i.e. a throat-like structure, where a transition between the two regions takes place. This was achieved by means of a modified radial function, which smoothly interpolates from the standard Ellis case to the bounded 2-sphere core on the other side.

In the internal region of the modified EBWH, the areal radius exhibits a local maximum and eventually collapses to its asymptotic value R. Such a peculiar behavior is ultimately responsible for a rich geodesic structure. We performed an extensive analysis on causal geodesics, finding that regardless of the model parameters, the modified EBWH is geodesically complete, even in the vanishing asymptotic 2-sphere scenario, $R = 0$. This is indeed relevant, because in the vanishing 2-sphere radius case, the curvature scalars, energy density and pressures are unbounded as $x \to -\infty$, but these divergences remain unreachable for causal geodesics. In the $R \neq 0$ scenario, the curvature scalars are well defined everywhere and go to those of a 2-sphere with radius R in the asymptotic internal region.

We also investigated photon orbits in this model by numerically solving the geodesic equation. When the asymptotic value of the 2-spheres radius is lower than the throat radius, $R < a$, there are light rays that depending on their impact parameter suffer a bounce in the inner universe and are scattered back to the outer universe. As R diminishes, and the inner region becomes more bounded, the photon's impact parameter necessary for the bounce to happen is smaller (see Fig. 9). The extreme scenario is then for $R = 0$, where all geodesics entering the inner universe are scattered back to the outer one, and the only null geodesic that can propagate forever in the inner region is that of a photon in purely radial motion. Last, for $R \geq a$, any photon that crosses the throat propagates towards the asymptotic infinity with a bounded 2-sphere radius.

The analysis of the effective potential shows that an unstable photon sphere is present at the throat, similarly to the standard EBWH. Moreover, the inner universe has an additional structure, a stable photon sphere, that is located in the local minimum of the effective potential. The existence of the stable photon sphere allows long-lived modes to be trapped, giving rise to the appearance of echoes in the ringdown profile, usually absent in standard EBWHs. In order to probe this aspect, we performed an analysis of massless scalar excitations in the modified EBWH background. After being transmitted to the inner universe the scalar perturbation interacts with an effective centrifugal barrier for $R = 0$ or a step potential for $R \neq 0$. Therefore, part of the modes are trapped in a potential well and observed as a series of echoes in the time profile of the scalar perturbation. In particular, we noticed that the role of the parameter c is to modify the time delay between two successive echoes. When c increases, the cavity in the effective potential becomes narrower and the echoes' time delay diminishes.

The role of the asymptotically bounded 2-sphere radius R is more subtle. For the $R = 0$ case, the scalar perturbations get trapped between the unbounded barrier and the photon sphere at the throat. By increasing R, this behavior persists, but since the unbounded barrier is replaced by a step potential barrier, part of the modes can be transmitted through the asymptotic internal region.

We notice that by replacing the asymptotically Minkowski spacetime with a bounded 2-sphere core, the scalar field acquires an effective mass in the asymptotic internal region for nonvanishing values of the multipole number ℓ and nonzero asymptotic 2-sphere radius R. A similar effect is observed with scalar waves propagating around magnetized black holes [63]. This leads to the presence of quasiresonances in the late-time profile, which are arbitrarily long-lived QNMs. If $R = 0$ and $\ell \neq 0$, the effective mass grows without bound acting as an effective mirror for the scalar wave. Consequently, the scalar perturbation cannot reach the asymptotic internal region, and the modes trapped near the stable photon sphere at some late time should tunnel to the outer universe.

Our results indicate that the observational features of wormholes are crucially dependent on their global characteristics, even though they can share a very similar throat-like structure. The study of perturbations can be used to extract valuable information about the compactness of the inner universe, and this could be useful in future spectroscopy experiments trying to identify new kinds of compact objects. We remark that the geometrical structure of the model described in the present work can be enriched further in multiple ways, such as by considering scenarios with horizons, or by restricting the domain of the bounded 2-sphere patch, i.e. truncating the range of the possible values spanned by the coordinate x and imposing specific boundary conditions, among other options. These configurations are expected to generate a great variety of phenomenological signatures in geodesic motions due to the appearance of additional potential barriers or closed universe effects. The study of such aspects is currently underway and will be the subject of forthcoming works.

ACKNOWLEDGMENTS

The authors would like to acknowledge Fundação Amazônia de Amparo a Estudos e Pesquisas (FAPESPA), Conselho Nacional de Desenvolvimento Científico e Tecnológico (CNPq) and Coordenação de Aperfeiçoamento de Pessoal de Nível Superior (CAPES)—Finance Code 001, from Brazil, for partial financial support. This work is supported by the Spanish Grant PID2020–116567 GB-C21 funded by MCIN/AEI/10.13039/501100011033, and the project PROMETEO/2020/079 (Generalitat Valenciana). This research has further been supported by the European Union's Horizon 2020 research and innovation (RISE) programme H2020-MSCA-RISE-2017 Grant No. FunFiCO-777740 and by the European Horizon Europe staff exchange (SE) programme HORIZON-MSCA-2021-SE-01 Grant No. NewFunFiCO-101086251. L. C. B. C. thanks University of Aveiro, in Portugal, for the kind hospitality during the completion of this work. R. B. M. thanks the Dept. of Theoretical Physics & IFIC of the University of Valencia & CSIC for the kind hospitality during the elaboration of this work. A. S. M.-F. is supported by the Spanish Ministerio de Ciencia e Innovación with the PhD fellowship PRE2018-083802. The work of F. B. is supported by the postdoctoral grant CIAPOS/2021/169 (Generalitat Valenciana).

[1] B. P. Abbott *et al.* (LIGO Scientific and Virgo Collaborations), Phys. Rev. Lett. **116**, 061102 (2016).
[2] K. Akiyama *et al.* (Event Horizon Telescope Collaboration), Astrophys. J. Lett. **875**, L1 (2019).
[3] C. A. R. Herdeiro and E. Radu, Phys. Rev. Lett. **112**, 221101 (2014).
[4] C. Herdeiro, E. Radu, and H. Rúnarsson, Classical Quantum Gravity **33**, 154001 (2016).
[5] I. Dymnikova, Gen. Relativ. Gravit. **24**, 235 (1992).
[6] S. Ansoldi, in Conference on Black Holes and Naked Singularities (2008), arXiv:0802.0330.
[7] S. L. Liebling and C. Palenzuela, Living Rev. Relativity **26**, 1 (2023).
[8] L. Visinelli, Int. J. Mod. Phys. D **30**, 2130006 (2021).
[9] P. O. Mazur and E. Mottola, Universe **9**, 88 (2023).
[10] M. Visser, *Lorentzian Wormholes: From Einstein to Hawking* (American Institute of Physics, New York, 1995).
[11] A. Simpson and M. Visser, J. Cosmol. Astropart. Phys. 02 (2019) 042.
[12] M. S. Morris and K. S. Thorne, Am. J. Phys. **56**, 395 (1988).
[13] J. Maldacena and L. Susskind, Fortschr. Phys. **61**, 781 (2013).
[14] K. K. Nandi, Y.-Z. Zhang, and A. V. Zakharov, Phys. Rev. D **74**, 024020 (2006).
[15] T. Ohgami and N. Sakai, Phys. Rev. D **91**, 124020 (2015).
[16] J. L. Blázquez-Salcedo, X. Y. Chew, and J. Kunz, Phys. Rev. D **98**, 044035 (2018).
[17] D.-C. Dai and D. Stojkovic, Phys. Rev. D **100**, 083513 (2019).
[18] J. H. Simonetti, M. J. Kavic, D. Minic, D. Stojkovic, and D.-C. Dai, Phys. Rev. D **104**, L081502 (2021).
[19] C. Bambi and D. Stojkovic, Universe **7**, 136 (2021).
[20] B. Azad, J. L. Blázquez-Salcedo, X. Y. Chew, J. Kunz, and D.-h. Yeom, Phys. Rev. D **107**, 084024 (2023).
[21] V. Cardoso, E. Franzin, and P. Pani, Phys. Rev. Lett. **116**, 171101 (2016); **117**, 089902(E) (2016).
[22] V. Cardoso, S. Hopper, C. F. B. Macedo, C. Palenzuela, and P. Pani, Phys. Rev. D **94**, 084031 (2016).
[23] M. Wielgus, J. Horak, F. Vincent, and M. Abramowicz, Phys. Rev. D **102**, 084044 (2020).
[24] M. Guerrero, G. J. Olmo, D. Rubiera-Garcia, and D. S.-C. Gómez, Phys. Rev. D **105**, 084057 (2022).
[25] J. Calderón Bustillo, N. Sanchis-Gual, A. Torres-Forné, J. A. Font, A. Vajpeyi, R. Smith, C. Herdeiro, E. Radu, and S. H. W. Leong, Phys. Rev. Lett. **126**, 081101 (2021).
[26] V. Cardoso and P. Pani, Living Rev. Relativity **22**, 4 (2019).
[27] M. Visser and D. Hochberg, Ann. Isr. Phys. Soc. **13**, 249 (1997).
[28] V. I. Afonso, G. J. Olmo, and D. Rubiera-Garcia, J. Cosmol. Astropart. Phys. 08 (2017) 031.
[29] R. B. Magalhães, A. Masó-Ferrando, G. J. Olmo, and L. C. B. Crispino, Phys. Rev. D **108**, 024063 (2023).
[30] A. Masó-Ferrando, N. Sanchis-Gual, J. A. Font, and G. J. Olmo, J. Cosmol. Astropart. Phys. 06 (2023) 028.
[31] A. Masó-Ferrando, N. Sanchis-Gual, J. A. Font, and G. J. Olmo, Phys. Rev. D **109**, 044042 (2024).
[32] H. G. Ellis, J. Math. Phys. (N.Y.) **14**, 104 (1973).
[33] K. Bronnikov, Acta Phys. Pol. B **4**, 251 (1973).
[34] R. B. Magalhães, A. Masó-Ferrando, F. Bombacigno, G. J. Olmo, and L. C. B. Crispino (to be published).
[35] V. Cardoso, S. Hopper, C. F. Macedo, C. Palenzuela, and P. Pani, Phys. Rev. D **94**, 084031 (2016).
[36] V. Cardoso and P. Pani, Nat. Astron. **1**, 586 (2017).
[37] P. Bueno, P. A. Cano, F. Goelen, T. Hertog, and B. Vercnocke, Phys. Rev. D **97**, 024040 (2018).
[38] K. A. Bronnikov and R. A. Konoplya, Phys. Rev. D **101**, 064004 (2020).
[39] M. Churilova, R. Konoplya, Z. Stuchlik, and A. Zhidenko, J. Cosmol. Astropart. Phys. 10 (2021) 010.
[40] Y. Yang, D. Liu, Z. Xu, Y. Xing, S. Wu, and Z.-W. Long, Phys. Rev. D **104**, 104021 (2021).
[41] V. I. Afonso, G. J. Olmo, E. Orazi, and D. Rubiera-Garcia, J. Cosmol. Astropart. Phys. 12 (2019) 044.
[42] R. B. Magalhães, L. C. Crispino, and G. J. Olmo, Phys. Rev. D **105**, 064007 (2022).
[43] M. K. Parikh, Phys. Rev. D **73**, 124021 (2006).
[44] W. Ballik and K. Lake, Phys. Rev. D **88**, 104038 (2013).
[45] V. Sharma and S. Ghosh, Eur. Phys. J. C **81**, 1004 (2021).
[46] S. Capozziello, T. Harko, T. S. Koivisto, F. S. N. Lobo, and G. J. Olmo, Phys. Rev. D **86**, 127504 (2012).
[47] E. I. Guendelman, G. J. Olmo, D. Rubiera-Garcia, and M. Vasihoun, Phys. Lett. B **726**, 870 (2013).
[48] C. Bambi, A. Cardenas-Avendano, G. J. Olmo, and D. Rubiera-Garcia, Phys. Rev. D **93**, 064016 (2016).
[49] A. Övgün, K. Jusufi, and I. Sakallı, Phys. Rev. D **99**, 024042 (2019).
[50] J. R. Nascimento, G. J. Olmo, P. J. Porfirio, A. Y. Petrov, and A. R. Soares, Phys. Rev. D **99**, 064053 (2019).
[51] J. a. L. Rosa, J. P. S. Lemos, and F. S. N. Lobo, Phys. Rev. D **98**, 064054 (2018).
[52] Z. Fu, B. Grado-White, and D. Marolf, Classical Quantum Gravity **36**, 045006 (2019); **36**, 249501(E) (2019).
[53] K. A. Bronnikov, Gravitation Cosmol. **25**, 331 (2019).
[54] R. B. Magalhães, A. Masó-Ferrando, G. J. Olmo, and L. C. B. Crispino, Phys. Rev. D **108**, 024063 (2023).
[55] M. Visser and C. Barcelo, in *Cosmo-99* (World Scientific, Singapore, 2000), pp. 98–112.
[56] E. Curiel, *Towards a Theory of Spacetime Theories* (Birkhäuser, New York, 2017).
[57] N. J. Cornish, Phys. Rev. D **64**, 084011 (2001).
[58] N. J. Cornish and J. Levin, Classical Quantum Gravity **20**, 1649 (2003).
[59] V. Cardoso, A. S. Miranda, E. Berti, H. Witek, and V. T. Zanchin, Phys. Rev. D **79**, 064016 (2009).
[60] H. Huang, J. Kunz, J. Yang, and C. Zhang, Phys. Rev. D **107**, 104060 (2023).
[61] C. Gundlach, R. H. Price, and J. Pullin, Phys. Rev. D **49**, 883 (1994).
[62] K. Kokkotas, R. Konoplya, and A. Zhidenko, Phys. Rev. D **83**, 024031 (2011).
[63] B. Turimov, B. Toshmatov, B. Ahmedov, and Z. Stuchlík, Phys. Rev. D **100**, 084038 (2019).
[64] A. Ohashi and M.-a. Sakagami, Classical Quantum Gravity **21**, 3973 (2004).
[65] R. A. Konoplya and A. Zhidenko, Phys. Lett. B **609**, 377 (2005).
[66] C.-Y. Shao, Y.-J. Tan, C.-G. Shao, K. Lin, and W.-L. Qian, Chin. Phys. C **46**, 105103 (2022).